ISTANBUL TECHNICAL UNIVERSITY ★ GRADUATE SCHOOL

INVESTIGATION OF THERMAL-FLOW PERFORMANCE IN CLOSE CIRCUIT COOLING TOWERS

M.Sc. THESIS

Efe GÜRLE

Department of Mechanical Engineering

Heat-Fluid Programme

DECEMBER 2025

ISTANBUL TECHNICAL UNIVERSITY ★ GRADUATE SCHOOL

INVESTIGATION OF THERMAL-FLOW PERFORMANCE IN CLOSE CIRCUIT COOLING TOWERS

M.Sc. THESIS

Efe GÜRLE
(503221122)

Department of Mechanical Engineering

Heat-Fluid Programme

Thesis Advisor: Prof. Dr. Tahsin ENGİN

DECEMBER 2025

İSTANBUL TEKNİK ÜNİVERSİTESİ ★ LİSANSÜSTÜ EĞİTİM ENSTİTÜSÜ

KAPALI ÇEVRİM SOĞUTMA KULELERİNDE TERMAL-AKIŞ PERFORMANSININ İNCELENMESİ

YÜKSEK LİSANS TEZİ

Efe GÜRLE
(503221122)

Makina Mühendisliği Anabilim Dalı

Isı-Akışkan Programı

Tez Danışmanı: Prof. Dr. Tahsin ENGİN

ARALIK 2025

Efe GÜRLE, a M.Sc. student of İTU Graduate School of Science Engineering and Technology student ID 503221122 successfully defended the thesis/dissertation entitled "INVESTIGATION OF THERMAL-FLOW PERFORMANCE IN CLOSE CIRCUIT COOLING TOWERS" which he prepared after fulfilling the requirements specified in the associated legislations, before the jury whose signatures are below.

Thesis Advisor :	**Prof. Dr. Tahsin ENGIN** Istanbul Technical University	....
Jury Members :	**Prof. Dr. Aliihsan KOCA** Istanbul Technical University	....
	Prof. Dr. Deniz ULUSARSLAN Yildiz Technical University	....

Date of Submission : 10 November 2025
Date of Defense : 5 December 2025

To my family,

FOREWORD

I would like to express sincere gratitude to Prof. Dr. Tahsin ENGIN for his invaluable guidance, encouragement, and continuous support throughout the course of this study. Special thanks are also extended to CENK Industry for providing access to experimental data, which significantly contributed to the validation and credibility of the numerical findings presented in this work.

Aralık 2025

Efe GÜRLE
(Thermal Systems Design
Engineer, TÜRKİYE)

TABLE OF CONTENTS

Page

ABBREVIATIONS

CFD	**:** Computational Fluid Dynamics
CCCT	**:** Closed-Circuit Cooling Tower
SST	**:** Shear Stress Transport
UDF	**:** User Defined Function
CSF	**:** Continuum Surface Force
HVAC	**:** Heating, Ventilating and Air Conditioning
CTI	**:** Cooling Tower Institute
RTD	**:** Resistance Temperature Detectors
VOF	**:** Volume of Fluid
DPM	**:** Discrete Phase Model
SIMPLE	**:** Semi-Implicit Method for Pressure Linked Equations

SYMBOLS

$\boldsymbol{A}$	: Heat or mass transfer area
$\boldsymbol{c_p}$	: Specific heat capacity
$\boldsymbol{d}$	: Diameter
$\boldsymbol{f}$	: Friction factor
$\vec{\boldsymbol{F}}$	: Force
$\boldsymbol{g}$	: Gravity
Re	: Reynolds number
$\boldsymbol{h}$	: Heat or mass transfer coefficient
$\boldsymbol{i}$	: Enthalpy
$\boldsymbol{m}$	: Mass
$\boldsymbol{n}$	: Specific number
Nu	: Nusselt number
$\boldsymbol{p}$	: Pressure
Pr	: Prandtl number
$\boldsymbol{S}$	: Source term
$\boldsymbol{T}$	: Temperature
$\vec{\boldsymbol{v}}$	: Velocity vector
$\boldsymbol{k}$	: Thermal conductivity
$\boldsymbol{\mu}$	: Dynamic viscosity
$\boldsymbol{\rho}$	: Density
$\boldsymbol{w}$	: Specific humidity
$\boldsymbol{\alpha}$	: Volume fraction
$\boldsymbol{L}$	: Length
$\boldsymbol{U}$	: Overall heat transfer coefficient
$\boldsymbol{t}$	: Time
$\boldsymbol{Y}$	: Mass fraction

$\boldsymbol{D}$	: Diffusion coefficient
$\boldsymbol{C}$	: Empirical mass transfer coefficient
$\boldsymbol{C_d}$	: Drag coefficient
$\boldsymbol{\tau_r}$	: Particle relaxation time
$\boldsymbol{G_k}$	: Generation of turbulence kinetic energy due to the mean velocity gradients
$\boldsymbol{G_b}$	: Generation of turbulence kinetic energy due to buoyancy
$\boldsymbol{\sigma}$	: Turbulent Prandtl number
$\boldsymbol{\varepsilon}$	: Rate of dissipation
$\boldsymbol{\kappa}$	: Turbulent kinetic energy
$\boldsymbol{\omega}$	: Spesific dissipation rate
$\boldsymbol{D_\omega}$	: Cross-diffusion term
$\boldsymbol{Y_\kappa}$	: Dissipation of turbulent kinetic energy due to turbulance
$\boldsymbol{Y_\omega}$	: Dissipation of spesific dissipation rate due to turbulance

SUBSCRIPTS

p	: Process
a	: Air
w	: Spray water
in	: Inner
o	: Outer
t	: Tube
al	: Overall
d	: Drag
i	: Species number
m	: Mixture
k	: Phase number
wv	: Water vapor
sat	: Saturation
ma	: Mean air
$masw$	: Mean air saturated water
tr	: Tubes per row
c	: circuit
log	: logarithmic
eff	: Effective
pt	: Particle
ε	: Rate of dissipation
κ	: Turbulent kinetic energy
ω	: Spesific dissipation rate

LIST OF TABLES

Page

LIST OF FIGURES

Page

INVESTIGATION OF THERMAL-FLOW PERFORMANCE IN CLOSE CIRCUIT COOLING TOWERS

SUMMARY

The main aim of this study is to investigate computational fluid dynamics (CFD) models to better understand the counter-current air–water interaction and thermal behavior in a packaged-type closed-circuit cooling tower (CCCT). The objectives of the study include examining key parameters such as flow behavior, specific humidity, water and air temperature, air velocity, heat transfer coefficient, pressure drop, and evaporation rate. To this end, both the Mixture multiphase method and the Discrete Phase Model (DPM) were implemented in two dimensions, while a three-dimensional DPM model was also developed to capture more realistic film distribution. The CFD results were validated by comparing the heat transfer coefficient between the water film and the outer tube surface with experimental data, aiming to provide a deeper understanding of heat and mass transfer mechanisms in CCCTs.

Initially, a two-dimensional CFD model using the Mixture multiphase method combined with the Shear Stress Transport (SST) k–ω turbulence model was tested to represent the air–water interface. However, this approach tended to overpredict evaporation and the spray-side heat transfer coefficient. Therefore, a more advanced two-dimensional DPM model was developed, which incorporated wall film boundary conditions, evaporation–condensation mass transfer, and species transport for water vapor diffusion. Simulations were performed in ANSYS Fluent using a structured mesh of approximately 160,000 elements, and the spray water was directed toward the coil surfaces to capture realistic film formation and evaporation dynamics.

Finally, the analysis was extended to a three-dimensional DPM model to overcome the uniform distribution assumption inherent in 2D simulations. The 3D approach was able to capture more detailed flow structures which strongly affect local heat and mass transfer. This model provided more physical fidelity in terms of film temperature, evaporation rate, and heat flux compared to the 2D model.

To support the numerical approach, an experimental study was conducted using a CCCT equipped with 10 rows of staggered serpentine tubes under real atmospheric conditions. During testing, inlet and outlet air temperatures were recorded to evaluate the cooling performance of the system. The heat transfer coefficient between the falling water film and the outer tube surface was determined using empirical correlations and resistance-based calculations. These experimentally obtained values were then used to validate the CFD model by comparing the numerical results with measured data, ensuring that the simulation accurately captured the air-water interaction and coupled heat-mass transfer processes within the cooling tower.

In terms of experimental data, the dry and wet bulb temperatures of inlet air were recorded as 29°C and 19.7°C, respectively. The process water entered the tower at 34.9°C and was cooled to 25.9°C at the outlet. Data were averaged over one hour under

steady-state conditions to ensure accuracy. The range and approach values were calculated as 6.97°C and 6.17°C, respectively.

Based on appropriate thermal resistance calculations, the spray heat transfer coefficient was determined to be 1163 W/m^2·K. The total evaporation loss observed in experiment was 0.54 m^3/h. However, spray heat transfer coefficient was found to be around 1526 W/m^2·K based on the simulation results. Simulation results showed slight agreement with experimental findings, with the heat transfer coefficient exhibiting an error margin of approximately 30%, which indicates that the heat transfer between the water film and the outer tube surface is adequately captured in the 3D model.

KAPALI ÇEVRİM SOĞUTMA KULELERİNDE TERMAL-AKIŞ PERFORMANSININ İNCELENMESİ

ÖZET

Bu çalışmanın temel amacı, paket tip kapalı devre soğutma kulesinde (CCCT) gerçekleşen karşı-akışlı hava–su etkileşimi ve buna bağlı ısıl davranışın daha kapsamlı bir şekilde anlaşılabilmesi için gelişmiş hesaplamalı akışkanlar dinamiği (CFD) modellerinin geliştirilmesi ve değerlendirilmesidir. Kapalı devre soğutma kuleleri hem endüstriyel proseslerde hem de HVAC uygulamalarında sürdürülebilir su yönetimi açısından kritik bir role sahiptir. Bu nedenle, bu tür sistemlerdeki karmaşık ısı ve kütle transfer mekanizmalarının doğru modellenebilmesi hem tasarım optimizasyonu hem de işletme performansının artırılması açısından büyük önem taşır. Bu çalışma kapsamında elde edilen sayısal ve deneysel bulgular, CCCT sistemlerinde sprey suyu, hava akışı ve serpantin yüzeyi arasındaki etkileşimlerin fiziksel olarak daha doğru temsil edilmesi yoluyla mevcut literatüre önemli katkılar sunmayı hedeflemektedir.

Çalışmanın odak noktası, akış davranışı, özgül nem, hava ve su sıcaklık dağılımları, hava hızı profilleri, ısı transfer katsayısı, basınç kaybı ve buharlaşma kaybı gibi temel performans parametrelerinin ayrıntılı incelenmesidir. Bu kapsamda ardışık olarak iki boyutlu Mixture çok fazlı modeli, iki boyutlu Ayrık Faz Modeli (DPM) ve son aşamada üç boyutlu DPM modeli uygulanmıştır. Her bir modelin fiziksel doğruluk, çözüm süresi ve film davranışını temsil etme kabiliyeti yönünden farklı avantaj ve sınırlamaları bulunmaktadır. Elde edilen sonuçlar, bu modellerin CCCT gibi karmaşık evaporatif soğutma sistemlerinde ne ölçüde güvenilir çıktılar üretebildiğini değerlendirmek amacıyla deneysel verilerle karşılaştırılmıştır. Özellikle serpantin yüzeyi ile su filmi arasındaki ısı transfer katsayısı, model doğrulamasında bir referans parametre olarak kullanılmıştır.

İlk aşamada, hava ve su fazlarının birlikte taşınmasını tanımlamak amacıyla, Shear Stress Transport (SST) k–ω türbülans modeli ile birleştirilmiş iki boyutlu Mixture multifaz yöntem incelenmiştir. Bu yaklaşım, genel akış davranışını başarıyla yakalayan bir yöntem olmasına rağmen, modelin doğası gereği sprey mekanizmasının fiziksel gerçekliğini temsil etmede yetersiz kalmaktadır. Mixture modeli, havanın doyma sıcaklığı altındaki buharlaşma süreçlerini ve serpantin borusu çevresindeki özgül nem dağılımını doğru şekilde modelleyememiştir. Özellikle sprey bölgesindeki buharlaşma hızının ve buna bağlı olarak sprey tarafı ısı taşınım katsayısının gerçeğe göre yüksek tahmin edildiği gözlemlenmiştir.

Bu nedenle çalışma, daha ayrıntılı fizik modellerine sahip iki boyutlu bir DPM yaklaşımına yönelmiştir. 2D DPM modeli, damlacıkların tek tek izlenmesine olanak tanıdığı için sprey suyu davranışını ve buharlaşma mekanizmalarını çok daha gerçekçi şekilde temsil eder. Geliştirilen model, duvar filmi oluşumu, damlacık çarpmasıyla film kalınlığının değişimi, buharlaşma miktarı ve su buharının hava fazına difüzyonu gibi çok önemli fiziksel süreçleri kapsayacak şekilde yapılandırılmıştır. Bu doğrultuda ANSYS Fluent ortamında yaklaşık 160.000 elemandan oluşan yüksek çözünürlüklü

bir ağ kullanılmış, serpantin yüzeyine ulaşan su damlacıklarının boru yüzeyine tutunabilmesi ve bir film oluşturabilmesi için duvar-film (wall-film) modeli aktif edilmiştir. Böylece 2D DPM analizleri, Mixture modeline kıyasla film dağılımını, yüzey ıslaklığını ve buharlaşma hızını çok daha gerçekçi şekilde temsil etmiş ve ısı taşınım katsayısının fiziksel olarak daha doğru hesaplanmasını sağlamıştır.

Ancak iki boyutlu bir yaklaşımın doğası gereği spreyin üç boyutlu dağılım özelliklerini ve serpantin boruları arasındaki karmaşık akış yapılarının tümünü temsil etmesi mümkün değildir. Bu nedenle çalışma, son aşamada üç boyutlu bir DPM modeline genişletilmiştir. 3D model, film dağılımının gerçekçi şekilde yakalanmasını sağlayan daha ayrıntılı akış alanları içermektedir. Bu model, 2D modele kıyasla film sıcaklığı, buharlaşma miktarı ve ısı akısı açısından daha fiziksel olarak gerçekçi sonuçlar sağlamıştır. Bu durum, CCCT gibi karmaşık sistemlerde üç boyutlu DPM modellerinin doğruluğunu önemli ölçüde artırmaktadır.

Sayısal yaklaşımı desteklemek amacıyla, 10 sıralı şaşırtmalı serpantin içeren bir CCCT sistemi üzerinde gerçek atmosfer koşullarında deneysel bir çalışma gerçekleştirilmiştir. Deneylerde giriş ve çıkış proses sıcaklıkları kaydedilmiş, sprey suyu sıcaklıkları ölçülmüş ve sistem kararlı hale geldikten sonra tüm verilerin bir saatlik ortalaması alınmıştır. Dış boru yüzeyi ile su filmi arasındaki ısı transfer katsayısı, deneysel korelasyonlar ve ısıl direnç esaslı hesaplamalar kullanılarak belirlenmiştir. Bu deneysel veriler, CFD modelinin doğrulamasında kullanılmış ve sayısal sonuçlarla karşılaştırılarak modelin hava-su etkileşimini ve ısı-kütle transferini ne ölçüde doğru temsil ettiği değerlendirilmiştir.

Deneysel verilere göre, giriş havasının kuru termometre sıcaklığı 29°C ve yaş termometre sıcaklığı 19,7°C olarak ölçülmüştür. Proses suyu kuleye 34,9°C sıcaklıkla girmiş ve çıkışta 25,9°C'ye kadar soğutulmuştur. Sprey sıcaklığı ise 24,7°C olarak elde edilmiştir. Elde edilen "sıcaklık farkı" ve "yaklaşım" değerleri sırasıyla 6,97°C ve 6,17°C olarak hesaplanmıştır.

Dış boru yüzeyi ile su filmi arasındaki ısı transfer katsayısı, deneysel korelasyonlar, literatür tabanlı film ısıl direnç modelleri ve ölçülen sıcaklık farkları kullanılarak 1163 $W/m^2 \cdot K$ olarak elde edilmiştir. Deneysel olarak gözlemlenen toplam buharlaşma kaybı ise 0.54 m^3/h'tir. Ancak, simülasyon sonuçlarına göre bu değer yaklaşık 1526 $W/m^2 \cdot K$ olarak bulunmuştur. Simülasyon sonuçları, deneysel bulgularla kısmi bir, uyum göstermiş ve ısı transfer katsayısında yaklaşık %30'luk bir fark tespit edilmiştir. Bu durum, su filmi ile dış boru yüzeyi arasındaki ısı transferinin 3D modelde yeterli doğrulukta yakalandığını göstermektedir.

Bu çalışma kapsamında elde edilen bütün deneysel ve sayısal bulgular birlikte değerlendirildiğinde, kapalı devre soğutma kulelerinde gerçekleşen çok fazlı ısı ve kütle transferinin son derece karmaşık, güçlü biçimde bağlaşık ve üç boyutlu karaktere sahip bir süreç olduğu açıkça görülmüştür. Gerçek sistem davranışının, özellikle su filmi dağılımı, damlacıkların serpantinle etkileşim dinamikleri, yerel buharlaşma bölgeleri ve akış yönüne bağlı ıslanma süreksizlikleri gibi karmaşık fiziksel mekanizmalara duyarlı olduğu ortaya çıkmıştır. Sayısal analizler, bu mekanizmaların doğru temsil edilmesinin yalnızca fazlar arası etkileşimlerin ayrıntılı bir biçimde modellenmesiyle mümkün olabileceğini, özellikle de sprey-su/film-su ilişkilerinin serpantin geometrisi boyunca homojen olmayan bir yapı sergilediğini göstermiştir.

Bu çalışma hem deneysel yaklaşım hem de gelişmiş CFD yöntemleri aracılığıyla, CCCT sistemlerinde su filmi, damlacık hareketi ve hava akışı arasındaki çok yönlü etkileşimlerin fiziksel doğasına ilişkin kapsamlı bir çerçeve sunmuştur. Elde edilen sonuçlar, kapalı devre soğutma kulelerinde tasarım optimizasyonu, performans iyileştirmesi ve daha güvenilir mühendislik hesaplamaları açısından değerli bir referans niteliği taşımakta; bundan sonraki çalışmalara ise tam ölçekli 3D çözümler, zamana bağlı analizler ve daha gelişmiş damlacık-film etkileşim modellerinin dâhil edilmesi yönünde net bir yol haritası oluşturmaktadır.

1. INTRODUCTION

Despite the fact that package-type cooling towers are commonly used in HVAC systems—particularly in applications such as hospitals, shopping malls, hotels, and industrial facilities—computational fluid dynamics studies focusing on these systems remain quite limited in the literature. Closed-circuit cooling towers, in particular, present a range of modeling challenges due to the complex and simultaneous interactions of heat and mass transfer processes. These interactions include convective heat exchange, phase change (evaporation and condensation), and multiphase flow behavior, which occur within a highly coupled system involving air, water, and internal process fluid.

Unlike open cooling towers, where the water is directly exposed to the atmosphere, closed-circuit systems circulate a process fluid within a sealed coil, while spray water and air flow over the external surface of the tubes. This configuration improves hygiene and system efficiency but introduces significant modeling difficulties. The spray water forms a falling film over the tube bundle while the counterflowing air interacts with this film to facilitate evaporative cooling. The heat transfer mechanisms in this setup involve both sensible heat exchange (due to temperature differences) and latent heat transfer (due to evaporation), making the system behavior highly nonlinear and sensitive to boundary conditions.

Due to these complexities, most engineering applications rely on empirical correlations or simplified design charts rather than fully detailed numerical simulations. However, with the increasing availability of computational power and the development of robust CFD models, there is growing interest in using simulation-based approaches to better understand and optimize the performance of CCCTs.

1.1 Purpose of Thesis

This study aims to contribute to growing body of cooling tower research by developing a CFD model to investigate the thermal-flow behavior in a closed-circuit cooling tower and to validate the model results against experimental data provided by industry. By comparing theoretical and numerical results, the study also seeks to identify the limitations of current modeling approaches and provide insights for future improvements in simulation accuracy.

1.2 Scope of Thesis

This thesis is structured into four main chapters, each addressing a specific aspect of the investigation on the thermal and fluid dynamic behaviour of a packaged-type Closed-Circuit Cooling Tower. The overall aim is to provide a comprehensive understanding of the coupled heat and mass transfer mechanisms between the air and water phases through both experimental and numerical analyses.

Chapter 1 – Introduction provides the fundamental background and motivation for the study. It outlines the importance of cooling technologies in industrial and HVAC applications, emphasizing the need for improved efficiency and accurate modeling of closed-circuit cooling towers. The objectives of the thesis are outlined in Section 1.1. Section 1.3 provides a general overview of cooling towers, describing their types, the placement of closed-circuit cooling towers within these classifications, and their main areas of application. Section 1.4 then presents a comprehensive literature review summarizing previous experimental and computational studies on evaporative heat transfer and multiphase flow modeling in similar systems. The chapter concludes by identifying the existing research gaps and defining the overall scope of the present study.

Chapter 2 – Methodology explains in detail the experimental setup, mathematical formulation, and computational modeling strategies adopted in this research. Section 2.1 describes the experimental facility, data acquisition process, and measurement techniques used to evaluate the performance of the CCCT under various operating conditions. Section 2.2 presents the mathematical model of the system, including the governing equations, thermophysical property correlations, and assumptions applied to simplify the physical problem. Section 2.3 focuses on the Computational Fluid Dynamics (CFD) modeling approaches. Three separate simulation frameworks are introduced: the Mixture Multiphase Model, the 2D DPM, and the 3D DPM Model. Each configuration is explained in terms of mesh structure, boundary conditions, turbulence models, and phase interaction mechanisms. Finally, Section 2.4 includes the mesh independence analysis and validation procedures, where simulation results are compared with experimental data to assess numerical accuracy.

Chapter 3 – Results and Data Analysis presents and discusses both experimental and numerical findings in a comparative manner. Section 3.1 summarizes the experimental outcomes, including variations in temperature, humidity, and evaporation rate under different air velocities. Section 3.2 provides detailed CFD results for each modeling approach. Subsection 3.2.1 discusses the performance of the Mixture Model, emphasizing its limitations in predicting film evaporation. Subsection 3.2.2 focuses on the 2D DPM simulations, which incorporate more realistic droplet tracking and wall-film interactions. Subsection 3.2.3 introduces the 3D DPM model, where more complex flow structures, non-uniform film distributions, and shadow regions are captured. A comparative analysis among all models highlights the evolution in predictive accuracy from 2D to 3D simulations.

Chapter 4 – Conclusion summarizes the main findings of the study, highlighting the accuracy and limitations of each numerical model compared to the experimental results. Recommendations for future work are provided, including suggestions for improving mesh resolution, implementing transient analysis, and extending the 3D simulations to full-scale tower geometries.

In addition to the main chapters, Appendices are included to provide supplementary data such as thermophysical properties of air, water vapor, and liquid water used in the simulations.

Overall, this thesis combines experimental measurements with advanced CFD techniques to enhance the understanding of coupled heat and mass transfer in CCCT systems, contributing to both academic research and practical design optimization.

1.3 Closed Circuit Cooling Towers

Cooling towers are essential components in industrial and HVAC systems, designed to reject excess heat from a process or working fluid to the atmosphere. They operate on the principle of heat exchange between air and water, utilizing sensible heat transfer, latent heat transfer, or a combination of both to lower the temperature of the working fluid. Depending on the design, cooling towers can be classified into several categories, including open-circuit (wet), closed-circuit (dry or hybrid), and mechanical or natural draft configurations.

The growing demand for energy-efficient and environmentally sustainable cooling systems has driven the development of advanced tower designs that minimize water consumption while maintaining high thermal performance.

Cooling towers can be broadly categorized based on heat exchange mechanism**,** air circulation method**,** and circuit configuration.

(1) Natural Draft Cooling Towers: Natural draft cooling towers rely on buoyancy forces to induce airflow without using mechanical fans. The hot, moist air inside the tower rises naturally due to density differences, drawing in cooler ambient air from the bottom. These towers are typically constructed with a hyperbolic shell structure, offering structural stability and high air circulation efficiency. They are mainly used in large-scale power plants and industrial facilities with high cooling loads. Advantages include low operational cost and minimal mechanical maintenance, though the construction cost and required space are significant.

(2) Forced Draft Cooling Towers: Forced draft cooling towers use fans located at the air inlet to push air through the fill media. The fan at the base of the tower ensures that air moves upward through the packing, enhancing the heat and mass transfer between air and water. This configuration provides precise airflow control but is more susceptible to recirculation of discharged moist air, especially in confined areas. Forced draft designs are typically applied in medium-sized industrial cooling systems and HVAC units.

(3) Induced Draft Cooling Towers: Induced draft towers use a fan at the top of the tower to draw air through the fill and exhaust it upward. This configuration minimizes recirculation and achieves better thermal performance compared to forced draft types. The uniform airflow distribution across the fill section improves the overall heat transfer efficiency. Induced draft towers are the most common mechanical-draft cooling systems in modern applications due to their balance between efficiency and reliability.

(4) Crossflow Cooling Towers: In crossflow configurations, air moves horizontally across the falling water. Water is distributed at the top through

spray nozzles or distribution basins and flows downward by gravity, while air is drawn horizontally through the fill media. This arrangement provides easy maintenance and uniform water distribution but can lead to non-uniform airflow and higher drift losses. Crossflow towers are common in HVAC and light industrial applications.

(5) Counterflow Cooling Towers: In counterflow cooling towers, air moves vertically upward against the downward flow of water. This counter-current contact enhances the temperature difference and increases heat and mass transfer efficiency. However, this design requires higher fan power due to increased air pressure drop. Counterflow towers are often preferred in space-limited installations and applications demanding high cooling efficiency.

(6) Open-Circuit Cooling Towers: Open-circuit cooling towers directly expose process water to ambient air. The water is sprayed over fill media, enhancing surface area for evaporation. As the water evaporates, it releases latent heat and becomes cooler before being collected in the basin. Although open towers are cost-effective and simple, they suffer from water loss, contamination, and scaling issues due to direct air contact.

(7) Closed-Circuit Cooling Towers: Closed-circuit cooling towers employ a sealed heat exchanger coil through which process water circulates. Ambient air and spray water flow over the coil, cooling the internal process fluid indirectly through both convective and evaporative heat transfer.This configuration prevents contamination, and provides precise temperature control, making it suitable for HVAC chillers, data centers, and industrial processes requiring clean closed loops.

(8) Hybrid Cooling Towers: Hybrid cooling towers combine wet and dry cooling principles to optimize water usage and thermal efficiency. Under low ambient conditions, the system operates in dry mode using air alone; under high loads, it switches to wet evaporative cooling to enhance heat rejection. Hybrid systems are increasingly adopted in water-scarce regions and energy-efficient plants, balancing environmental sustainability and performance.

Among these, Closed-Circuit Cooling Towers have gained significant attention for their ability to combine the advantages of both wet and dry cooling systems, offering high reliability, compact design, and low contamination risk. CCCTs are widely used in sectors where fluid purity, reliability, and space efficiency are crucial. Common applications include: HVAC and refrigeration systems in commercial buildings, industrial process cooling (chemical, food processing, power plants), data centers and electronic cooling systems, renewable energy systems such as geothermal or solar-assisted chillers, air compressor and injection molding unit cooling.

In modern industry, their ability to provide compact design while maintaining high cooling performance has made CCCTs a preferred alternative to conventional wet cooling towers.

1.4 Literature Review

Since 1998, computational fluid dynamics studies have been applied to improve the understanding and performance of closed-circuit cooling towers. The early work by Gan and Riffat introduced a two-phase, two-dimensional CFD model using an Eulerian-Lagrangian approach to evaluate CCCT performance for chilled ceiling systems. Their work also includes water droplet trajectories by using a dispersed phase model to simulate sprayers. Their simulation showed that CFD could predict cooling tower behavior with adequate heat input and is useful for design optimization [1]. Their CFD simulation predict coil temperature in a good agreement with their measured data.

In a subsequent study, Gan et al. further applied two-dimensional CFD to predict the thermal and pressure drop performance of CCCTs, validating their model against both industrial and prototype systems. Their results confirmed CFD’s capability to evaluate the effects of single- and multi-phase flow behavior around heat exchangers [2]. They conclude that CFD simulations should include detailed models of heat and mass transfer to assess the temperature drop of chilled water but they address the limitations of simplified CFD setups and include variable heat fluxes based on experimental data.

Qiu et al. analyzed falling film behavior on horizontal tubes in desalination systems, comparing numerical results with experiments. Their findings highlighted how Reynolds number, tube diameter, and flow rate affect film thickness and potential dry-out regions [3]. However, unlike a typical cooling tower, their CFD model simulated air and water in a co-current flow, and the effect of evaporation was not considered.

Chen et al. simulated falling-film patterns over horizontal tube bundles, identifying five distinct flow regimes based on flow rate. Their results matched well with experiments and provided thresholds for transitions between flow modes [4]. Similarly, their CFD simulation modeled air and water flowing in the same direction. In studies on falling film behavior, the Volume of Fluid (VOF) method was preferred over the discrete phase model approach.

Fiorentino and Starace developed a 2D model for falling film evaporation, analyzing flow stability and transitions influenced by tube spacing and water-to-air mass flow ratios. They proposed a trade-off curve to avoid film break-up in evaporative condensers [5]. Their work analyzes the falling film evaporation in evaporative condensers but except the fluid inside the tubes, the physics of simulation is actually same with the closed-circuit cooling towers.

Xie et al. compared plain, finned, and oval tubes using CFD coupled with the discrete phase model and species transport. The oval tube design showed optimal thermal-hydraulic performance with minimal pressure drop [6].

In a second study, Xie et al. investigated the effects of fin geometry and inlet air conditions on CCCT performance using field synergy theory. They systematically varied the number of fins and the angles at which air entered the system. The analysis revealed that increasing the fin number led to more complex flow interactions, enhancing the synergy between velocity and temperature fields. Optimizing the inlet air angle further improved turbulence intensity, which promoted better heat and mass transfer. Their findings emphasized the importance of matching structural geometry with fluid dynamics for improved system efficiency. Overall, this study provided practical guidance for designing CCCTs with higher thermal performance through geometric optimization [7].

Xie et al. (third study) developed a 3D CFD model of CCCTs using the Volume of Fluid (VOF) method and the SST k-omega turbulence model. Their goal was to better understand the distribution and dynamics of the falling water film along the heat exchanger surface. The simulations allowed them to analyze how water spread circumferentially around tubes, highlighting regions to uneven film thickness. Results showed that both spray density and inlet air velocity played critical roles in determining the film's uniformity and evaporation rate. Higher spray density generally improved film coverage, while increased air velocity enhanced evaporation by boosting convective effects. These insights offer valuable strategies for improving water distribution and evaporation efficiency in CCCTs [8].

Zhao et al. proposed an elliptical finned tube design aimed at improving the overall thermal performance of CCCTs. Using CFD analysis, they assessed the aerodynamic and thermal behavior of the new geometry in comparison with traditional circular tubes. The elliptical design demonstrated more uniform velocity distribution across the heat exchanger surface, which in turn reduced localized dry-out zones. Additionally, the improved airflow reduced pressure losses, contributing to lower fan energy consumption. These benefits translated into a measurable improvement in both cooling effectiveness and operational efficiency. The study highlighted how geometric modifications at the component level can lead to significant system-wide enhancements [9].

Liu et al. introduced the concept of a multi-mode cooling tower that dynamically adjusts operation based on environmental conditions. To support this idea, they developed a stochastic simulation-optimization framework capable of handling variable weather data. This model combined probabilistic inputs with CFD simulations to evaluate system behavior under multiple scenarios. The results demonstrated that the multi-mode design significantly increased exergy efficiency without excessively raising computational cost. In particular, the model adapted well to fluctuating ambient temperatures and humidity levels, making it suitable for real-world applications. This approach offers a new perspective on intelligent cooling tower design using adaptive simulation tools [10].

Heyns and Kröger focused on experimental investigations in CCCT research. They performed tests on evaporative coolers with deluged tube bundles to collect empirical data on heat and mass transfer coefficients [11]. Their experiments also measured pressure drops under various operational conditions to validate theoretical models. The collected data filled a gap in the literature, especially for deluged systems that had limited prior empirical analysis. Their correlations provided fundamental experimental support for both model development and practical design.

Wickert and Prokop conducted a comprehensive review of CFD tools used for simulating natural evaporation in cooling towers. They compared the performance of mesh-based methods like finite volume and finite element approaches with mesh-free alternatives such as smoothed particle hydrodynamics. They argued that despite advancements, purely physical models often fail to fully capture evaporation dynamics, especially at the microscale. As a result, artificial enhancements are often necessary to achieve reliable results. Their work underlines the importance of combining numerical innovation with practical constraints in simulation design [12].

The following works are also worth mentioning, Poppe and Merkel [14,15] laid the foundational groundwork for evaporative cooler modeling, followed by experimental studies on deluged tube bundles of various diameters and arrangements by Mizushina et al. [16], Parker & Treybal [17], and Niitsu et al. [18], which yielded key insights into film and mass transfer coefficients as well as air-side pressure losses across plain and finned geometries. A simplified analytical model coupled with stochastic bi-objective optimization improves the design robustness of closed wet cooling towers under weather variability [19], while new effectiveness–NTU correlations allow for accurate, non-iterative thermal predictions validated by experiments [20]. Enhancements in tube geometry, such as elliptical finned or oval tubes, offer superior thermal-hydraulic performance compared to traditional circular ones, boosting energy efficiency and cooling effectiveness [21,22]. Thermodynamic and numerical models reveal that inlet air conditions—especially wet bulb temperature and humidity—have significant impacts on CCCT thermal performance and water loss [23,24]. Recent experimental comparisons confirm the accuracy of Poppe and Merkel models, alongside novel empirical correlations, in predicting outlet temperatures and water consumption in CSP-integrated systems [25]. In building applications, closed wet cooling towers adapted for chilled ceilings demonstrate reliable performance when using experimentally derived transfer coefficients [26]. Data-driven reduced-order models combining PCA and neural networks enable fast and efficient exergy field optimization in CCCTs under uncertainty [27], while exergy analyses emphasize the need for matched inlet parameters to minimize irreversibility in heat and mass transfer [28,29]. For HVAC and hybrid ground source heat pump systems, exergy-based constrained optimization using genetic algorithms effectively reduces entropy generation while meeting load demands [30].

Some of the reviewed studies, such as those by Xie et al. and Fiorentino and Starace, focused on evaporative condensers or mostly used co-current flow, which is different from the closed-circuit cooling towers work. of the spray film–tube heat transfer coefficient with experimental results.

On the other hand, several studies have investigated the thermal and aerodynamic behavior of open-circuit and natural draft cooling towers. Meroney applied CFD to predict droplet drift and deposition from both mechanical and natural draft towers, showing good agreement with field experiments [31]. Al-Waked and Behnia simulated heat and mass transfer in a natural draft wet cooling tower using a combined Eulerian–Lagrangian approach, finding that crosswinds above 7.5 m/s enhance tower performance [32]. Hajidavalloo and Shakeri used a mathematical model to study crossflow cooling towers under variable wet-bulb conditions, revealing that higher humidity increases evaporation loss and range [33]. Chen et al. experimentally investigated the influence of cross walls under crosswind conditions in natural draft wet cooling towers, finding that properly oriented walls can significantly mitigate performance degradation at low wind speeds [34]. Blain et al. developed and validated an ANSYS Fluent-based CFD model for a large natural draft wet cooling tower, incorporating Poppe and Merkel formulations and achieving strong agreement with full-scale measurements [35]. Xia et al. analyzed pre-cooling water spray systems in natural draft dry towers and demonstrated that vertically arranged nozzles yield superior evaporation compared to horizontal ones [36]. Raoult et al. proposed a two-step CFD spray model to study polydisperse droplet evaporation, achieving accurate temperature predictions and reduced computational cost [37]. Guo et al. introduced new explicit analytical solutions for coupled heat and mass transfer in cooling tower systems, enabling rapid prediction of temperature and humidity profiles [38]. Chen et al. numerically examined the impact of non-equidistant fillings in large wet cooling towers and identified an optimal inner radius configuration that maximized cooling efficiency and airflow uniformity [39]. Zhang et al. extended this approach through a synergetic optimization of non-equidistant fillings and non-uniform water distribution, achieving up to 7% improvement in ventilation rate and reduced evaporation losses under design conditions [40]. Yu et al. developed a comprehensive coupling model integrating spray, rain, and packing zones in counter-flow towers, reducing predictive error to 3.25% compared with experiments [41]. Zhengqing Zhang et al. analyzed the effect of dry–wet hybrid rain zones on the heat and mass transfer characteristics of super-large natural draft wet cooling towers, showing that the hybrid configuration enhanced the volumetric heat transfer coefficient of the rain zone by over 16% while reducing evaporation losses at high crosswinds [42]. Yang et al. performed 3D CFD analysis on wet towers with multi-pitch fillings, finding that optimized fill layouts improved cooling efficiency by over 1% [43]. Castiglione et al. investigated part-load operation of an induced-draft open-circuit tower using CFD and found that energy consumption could be reduced by nearly 50% while maintaining design performance [44].

In addition, research has also been conducted on evaporative spray cooling systems, which share similar heat and mass transfer mechanisms with open-type cooling towers. Tissot et al. performed a numerical analysis of air cooling by evaporating droplets in the upward flow of a condenser, employing an Eulerian–Lagrangian framework. The study demonstrated that fine droplets (25–50 μm) could achieve up to 10 °C of air temperature reduction, emphasizing the nonlinear coupling between droplet size, dispersion, and evaporation behavior [45]. Lacour et al. developed a 3D spray dispersion model to evaluate the wetted surface area of heat exchangers exposed to water sprays. Their findings highlighted the sensitivity of wetting efficiency to droplet dispersion radius and evaporation rate, providing design insights for optimal nozzle positioning [46].

Finally, several studies have assessed the thermodynamic performance of cooling systems using exergy-based methods, offering a more comprehensive evaluation than conventional energy analysis. Ren et al. introduced an analytical framework for exergy analysis in HVAC systems, emphasizing its capability to quantify irreversibilities and the theoretical limits of evaporative cooling [47]. Kanoglu et al. performed a combined energy and exergy analysis of an open-cycle desiccant cooling system, showing that exergy evaluation effectively identifies components with major losses, such as the desiccant wheel and heating section [48]. Qureshi and Zubair applied the second law of thermodynamics to evaluate wet cooling towers and evaporative heat exchangers, demonstrating that higher inlet wet-bulb temperatures can enhance overall exergy efficiency [49]. Similarly, Muangnoi et al. developed a mathematical exergy model for a counterflow wet cooling tower and reported that the lowest exergy destruction occurred at the tower top, indicating reduced thermodynamic irreversibility along the tower height [50]. These studies on open-type wet cooling towers have provided extensive insights into the interplay of aerodynamic, thermal, and thermodynamic factors governing evaporative heat rejection.

In this study, a CFD model was developed employing a two-dimensional mixture multiphase and DPM approach to simultaneously investigate heat and mass transfer phenomena. The model represents a counter-current configuration between the air and water phases, by combining SST k - ω turbulence equations in the Fluent software. Realistic tower geometry and boundary conditions were implemented to enhance simulation. The main contribution of this study is the investigation of water evaporation effects on falling film flow and the comparison

2. METHODOLOGY

2.1 Experimental Procedure and Data Acquisition

To evaluate the thermal performance of the closed-circuit cooling tower under realistic operating conditions, a full-scale field test was conducted at a dedicated test facility located in Düzce, Türkiye. This facility is operated by Cenk Endüstri Tesisleri İmalat ve Taahhüt A.Ş., a leading Turkish company specializing in industrial cooling technologies.

Cenk Endüstri is the only company in Türkiye certified by Eurovent and CTI standards for its closed-circuit cooling towers, and its test site adheres to internationally recognized standards.

The subject of the test was a single-cell, induced-draft, counterflow-type closed-circuit cooling tower using water as the process fluid. The coil section consists of 20 rows, each composed of 36 tubes, providing a compact and efficient heat exchanger surface. Tubes are arranged with a transverse pitch of 56 mm and a longitudinal pitch of 48 mm, forming a staggered configuration to enhance heat and mass transfer. The air velocity through the tower is maintained at 3.5 m/s, while the spray water application rate is 4.2 L/s·m^2. The detailed specifications of the cooling tower, including design parameters, pump data, electrical data, fan data, and material data, are provided (see Tables 2.1–2.5).

The experimental methodology adhered to the standards and procedures defined by the Cooling Technology Institute (CTI), including CTI STD-201 for performance certification and ATC-105 for data acquisition practices.

Table 2.1 : Design Parameters.

Name	Data	Unit
Coil Configuration	20 rows × 36 tubes	-
Coil Width	2016	mm
Coil Length	4210	mm
Transverse Tube Pitch	56	mm
Longitudinal Tube Pitch	48	mm
Air Velocity	3.5	m/s
Spray Water Rate	4.2	$L/s \cdot m^2$
Coil Arrangement	Staggered	-
Heat Exchanger Surface Area	256	m^2
Pass Number	10	-
Anti-Freeze Ratio	0	%
Outer Tube Diameter	26.9	mm

All key thermal parameters were precisely measured using calibrated platinum resistance temperature detectors (RTDs), while data collection was handled through a multi-channel logging system integrated with a data analysis computer. Circulating water flow rates were determined by an electro-magnetic flow meter to ensure accurate hydraulic measurements. Electrical power consumption by the fan motor was recorded using a digital clamp-on kilowatt meter. The inlet air temperature and relative humidity were measured by placing a hygrometer in front of the louver. A schematic representation of the cooling tower is shown in Figure 2.1.

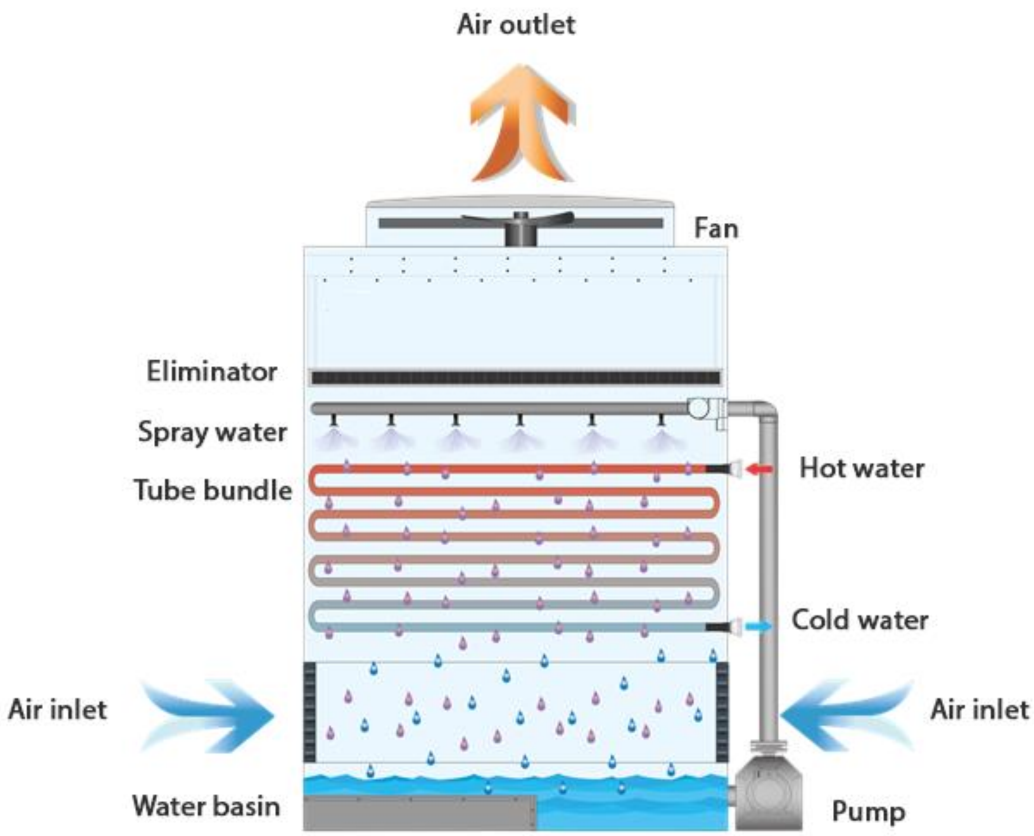

Figure 2.1 : Schematic presentation of the closed-circuit cooling tower.

The collected test data were then processed to identify stable time intervals for performance analysis. Among the 1-hour measurement intervals, the most stable period was selected for evaluation. During the selected time period, data were averaged and assessed in accordance with the analysis framework. A schematic representation of the experiment is shown in Figure 2.2.

Table 2.2 : Pump Data.

Name	Data	Unit
Pump Type	Monoblock Centrifugal	-
Pump Flow Rate	149	m^3/h
Number of Pumps	1	-

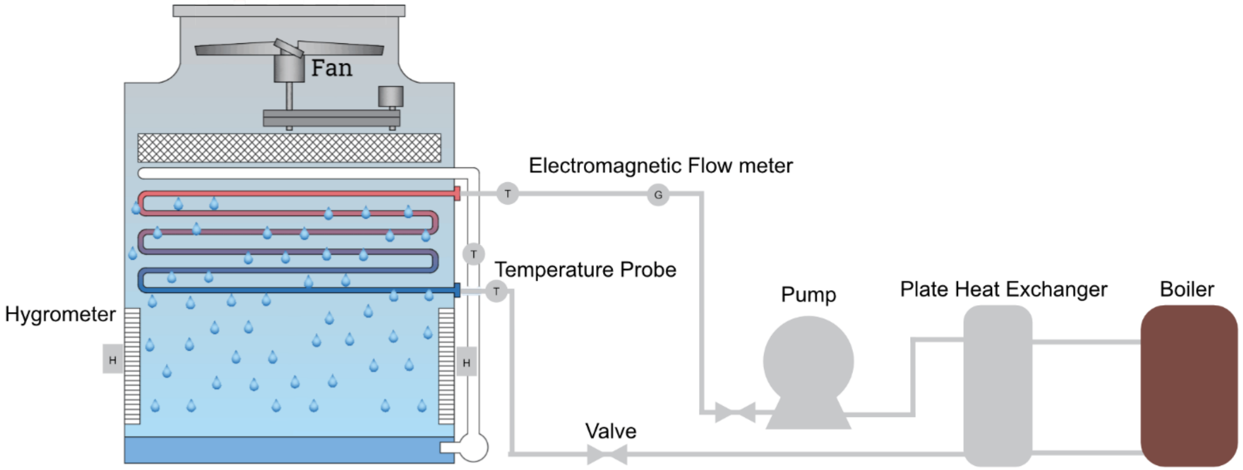

Figure 2.2 : Schematic presentation of of the utilized experimental system.

Table 2.3 : Electrical Data.

Name	Data	Unit
Fan Motor Shaft Power	21.29	kW
Fan Motor Nominal Power	2 x 15	kW
Pump Shaft Power	2.2	kW
Pump Nameplate Power	1 x 2.2	kW
Motor Voltage	400	V
Motor Efficiency Class	IE3	-
Motor Protection Class	IP55	-
Motor Isolation Class	F (155°C)	-

This experimental evaluation not only confirms compliance with CTI standards but also provides a reliable basis for validating the subsequent CFD model developed in this study.

Table 2.4 : Fan Data.

Name	Data	Unit
Total Air Flow	29.6	m^3/s
Number of Fans	2	–
Fan Diameter	2000	mm
Fan Drive System	Belt Driven	–
Fan Speed	960	rpm
Sound Pressure Level	113	dB
Sound Measurement Distance	15	m
Sound Power Level	78.5	dB(A)

Table 2.5 : Material Data.

Name	Material
Construction	Epoxy Coated Galvanized Steel (Z600)
Heat Exchanger	Hot Dip Galvanized Steel
Fan	Aliminiium
Eliminator	PVC
Water Distribution System	PVC
Nozzles	PP

The uncertainty in the spray side heat transfer coefficient was estimated through propagation of measurement errors associated with input parameters such as inlet/outlet temperatures, process water flow rate, and air conditions. By substitute each input within its respective uncertainty range, the overall uncertainty in h_w was found to be approximately ±6.7%. The uncertainties of these measured values are shown in Table 2.6.

Table 2.6 : Uncertainties of measurement and performance parameters [8].

Parameters	Uncertainty
Process water inlet temperature	±0.1 °C
Process water outlet temperature	±0.1 °C
Inlet air dry-bulb temperature	±0.2 °C
Inlet air relative humidity	±2.0 %
Process water mass flow rate	±1.0 %

2.2 Mathematical Modelling of the Closed-Circuit Cooling Tower

To evaluate the heat and mass transfer performance of the closed-circuit cooling tower, an algebraic approach was employed based on experimental observations. This method aims to estimate the spray-side heat transfer coefficient by processing known inlet air conditions, process water temperatures, and volumetric flow rates. Unlike the CFD analysis, this section provides a simplified 1D resistance-based thermal analysis.

In order to simplify the model while retaining physical significance, the following assumptions were made:

1- The water film flowing along the tube bundle maintains a uniform average film temperature throughout the entire cooling section. Since the process water is recirculated, the inlet and outlet water temperatures are assumed to be equal, neglecting minor internal gradients.

2- The air-water contact area is considered equivalent to the external surface area of the tube bundle.

3- The spray water is evenly distributed across all tube rows, ensuring total external surface wetting of the coil bundle.

4- Evaporation losses are considered negligible in the energy balance.

Model considers an elementary control volume of counter flow evaporative tube bundle as shown in the Figure 2.3.

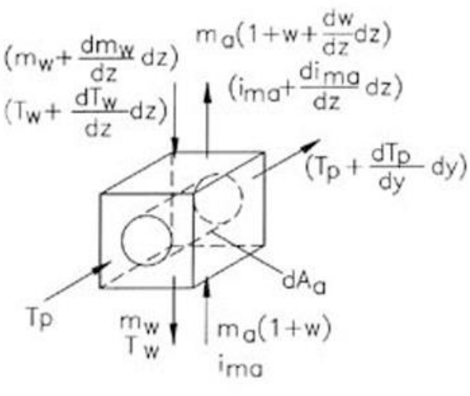

Figure 2.3 : Control volume of counterflow evaporative cooler [13].

Differential equation describes the enthalpy change of moist air (di_{ma}) as it flows over a wetted surface:

$$\dot{m}_a di_{ma} = h_d(i_{masw} - i_{ma})dA_a \quad (2.1)$$

where h_d is the mass transfer coefficient between the water surface and the air, i_{masw} and i_{ma} are the specific enthalpies of saturated air at the water temperature and the air inlet, respectively. dA_a is the differential air-water interface area, $\dot{m}_a$is the mass flow rate of the air. This formulation explains that the air gains enthalpy by absorbing water vapor through evaporation. The energy balance in the system is formulated using the principle of conservation of energy as follows:

$$\dot{m}_w c_{pw} dT_w = \dot{m}_a di_{ma} + \dot{m}_p c_{pp} dT_p \tag{2.2}$$

which is obtained after the first assumption:

$$\dot{m}_a di_{ma} + \dot{m}_p c_{pp} dT_p = 0 \tag{2.3}$$

where $\dot{m}_w$ is the mass flow rate of the water film, c_{pp} and c_{pw} are specific heat capacities of the process fluid and spray water, respectively, T_p is the temperature of the process fluid, T_w is the temperature of the spray water. Last differential equation defines the differential temperature drop (dT_p) of the process fluid flowing inside the tubes due to heat transfer with the surrounding water film:

$$\dot{m}_p c_{pp} dT_p = -U_a\left(T_p - T_w\right) dA_a \tag{2.4}$$

U_{al} is the overall heat transfer coefficient from the process fluid to the air stream through the water film.

$$U_{al} = \left[\frac{1}{h_w} + \frac{A_o}{A_{in} h_p} + \frac{d_o \, ln\left(\frac{d_o}{d_{in}}\right)}{2k_t} + \sum_n \frac{A_o}{A_n} R_n\right]^{-1} \tag{2.5}$$

where h_w is spray heat transfer coefficient, A_{in} and A_o are effective inner and outer surface area of the tube, d_o and d_{in} are outer and inner diameters of the tube, respectively, k is thermal conductivity coefficient of tube, R_n includes all other resistances (fouling, contact resistance if the outer surface is finned, etc.) between the waterfilm and the process fluid and h_p is convective heat transfer coefficient inside the process fluid. The fouling resistances for the inner and outer surfaces of the tube are provided in Table 2.7. The convective heat transfer coefficient inside the process fluid can be derived from the following expression:

$$h_p = \frac{\mathrm{Nu}_p k_t}{d_{in}} \tag{2.6}$$

where Nu_p is the Nusselt number of the pipe side. Nusselt number can be derived from the following expression:

$$\mathrm{Nu}_p = \frac{\left(\left(\frac{f_d}{8}\right)(\mathrm{Re}_p - 1000)\mathrm{Pr}_p \left(1 + \left(\frac{d_o}{L_t}\right)^{0.67}\right)\right)}{1 + 12.7\left(\frac{f_d}{8}\right)^{0.5} \left(\mathrm{Pr}_p{}^{0.67} - 1\right)} \tag{2.7}$$

where $\mathrm{Re_p}$ and $\mathrm{Pr_p}$ are Reynolds and Prandtl number of process water, respectively. Reynolds and Prandtl number of process fluid can be derived from the following expression:

$$\mathrm{Re}_p = \frac{m_p d_{in}}{A_{ts}\mu_p n_c n_{tr}} \tag{2.8}$$

$$\mathrm{Pr}_p = \frac{C_{pp}\mu_p}{k_p} \tag{2.9}$$

where A_{ts} is inner cross sectional tube area, μ_p is dynamic viscosity of process water, k_p is the thermal conductivity of process water, n_{tr} and n_c are the number of tubes per row and number of circuits, respectively. The properties of water and air used in the equations, as well as in the subsequent CFD analysis, are provided in Appendix A [13].

The performance parameter used to estimate the heat transfer coefficient between the spray water and air is expressed as follows:

$$h_{wa} = \frac{m_a c_{pa}}{A_o \Delta T_{log}}(T_{ao} - T_{ai}) = \frac{m_a c_{pa}}{A_o} \ln\left(\frac{(T_w - T_{ai})}{(T_w - T_{ao})}\right) \tag{2.10}$$

Where $\mathrm{T_{ai}}$ and $\mathrm{T_{ao}}$ are inlet and outlet temperature of air. The equations for estimating evaporation and blowdown losses are presented below in the given order:

$$Evaporation\ Loss = m_a(w_o - w_i) \tag{2.11}$$

$$Blowdown\ Loss = \frac{Evaporation\ Loss}{CoC - 1} \tag{2.12}$$

Where CoC refers to the cycle of concentration of water, which is typically taken as 3.5 for standard packaged-type cooling towers. These equations collectively form the basis of the heat and mass transfer model used to estimate the spray-side convective heat transfer coefficient. By sequentially solving the enthalpy change in air, the water film temperature variation, and the process fluid temperature drop, and by applying the overall heat transfer resistance formulation, the spray heat transfer coefficient was iteratively determined. This methodology provides a robust algebraic approach to quantify spray-side thermal performance in closed-circuit cooling towers based on experimentally measured inlet conditions and flow parameters.

Table 2.7 : Fouling resistance parameters used in the mathematical model [13,51].

Location	Fouling Resistance
Outer Surface ($m^2.K/W$)	$4.4\ x\ 10^{-5}$
İnner Surface ($m^2.K/W$)	$1.8\ x\ 10^{-5}$

2.3 CFD Domain and Numerical Setup

2.3.1 Mixture multiphase model CFD simulation setup

In this study, a two-dimensional computational fluid dynamics model was developed to investigate the coupled heat and mass transfer phenomena occurring in a closed-circuit cooling tower under counter-current flow conditions. The simulation framework employed the Mixture multiphase model available in ANSYS Fluent, which is suitable for capturing the interaction between liquid water, water vapor, and air phases.

To accurately resolve the flow and interfacial dynamics, the Shear Stress Transport turbulence model was adopted due to its performance in simulating near-wall behaviors and separation phenomena in multiphase flows. The computational domain represented a vertical slice of the cooling tower and was discretized using a fully structured quadrilateral mesh consisting of over 50,000 elements, as shown in Figure 2.4. This ensured a high-resolution capture of the flow features, particularly in regions near the tube surfaces and phase interfaces. Only the final row of serpentine coil tubes was modeled in order to simplify the geometry while still capturing the evaporation behavior. Water was given toward the center of the pipe surface to ensure a uniform film distribution over the coil. A schematic representation of the system is provided in Figure 2.5. Also, Figure 2.6 illustrates all boundary conditions applied to the CFD model.

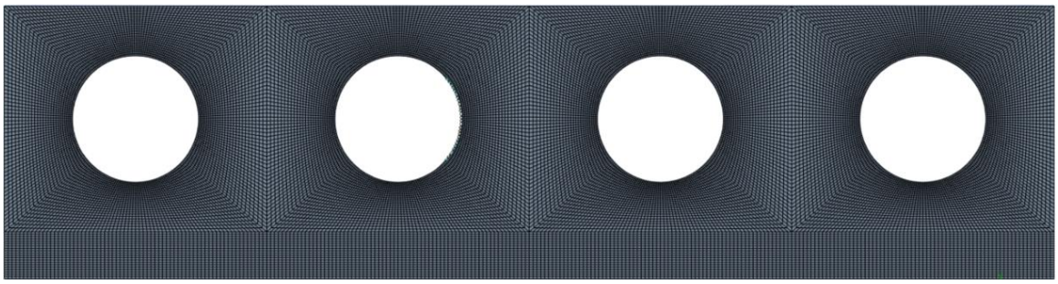

Figure 2.4 : The mesh structure of mixture model generated by Ansys Fluent.

To reduce computational cost while maintaining physical accuracy, the CFD model was simplified by focusing on a single spray nozzle. In the full-scale experimental setup, each spray covers a specific area of the coil bundle width, corresponding to approximately 4 out of the 36 total tubes. Therefore, the simulation domain was configured to represent a localized region comprising 4 horizontal tubes directly beneath one spray. The water mass flow rate was adjusted accordingly to reflect the actual discharge rate of a single nozzle, ensuring that the film distribution and heat-mass exchange observed in the simulation closely resemble those occurring in the physical system.

The simulations incorporated additional physical models to accurately describe humidification and phase change processes. Water vapor diffusion and advection were activated to represent air humidification. To enable evaporation at temperatures below the saturation point, a User-Defined Function (UDF) was developed and integrated with the Lee model for mass transfer. The volume fraction cutoff was set to minimum to maintain numerical stability.

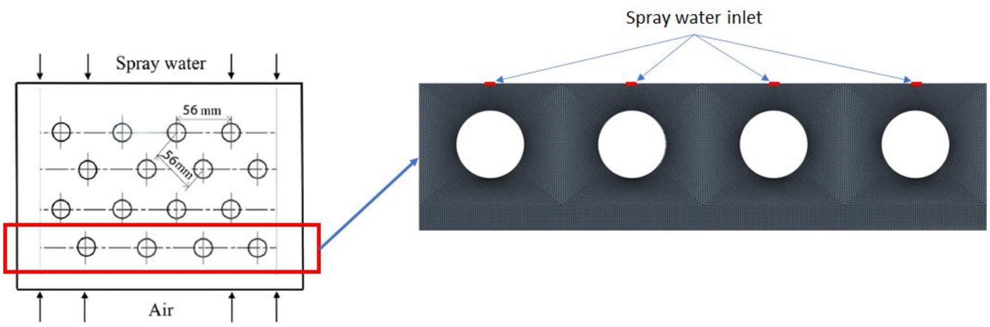

Figure 2.5 : Schematic presentation of the CFD mixture model.

Due to known overpredictions in phase change behavior when using the default dispersed flow model, the interface formulation was switched to a Sharp/Dispersed approach. The drag coefficient model that yielded the best numerical stability and convergence was the Symmetric model. Surface tension effects were included through the Continuum Surface Force model, and wall adhesion angles were defined as 90° to replicate the behavior of the falling film accurately. The slip velocity between phases was modeled following the Manninen et al. method, which provides a suitable approximation for gas-liquid interactions in stratified flow regimes. Detailed information about the model setup is provided in Table 2.8. The data related to the boundary conditions is shown in Table 2.9.

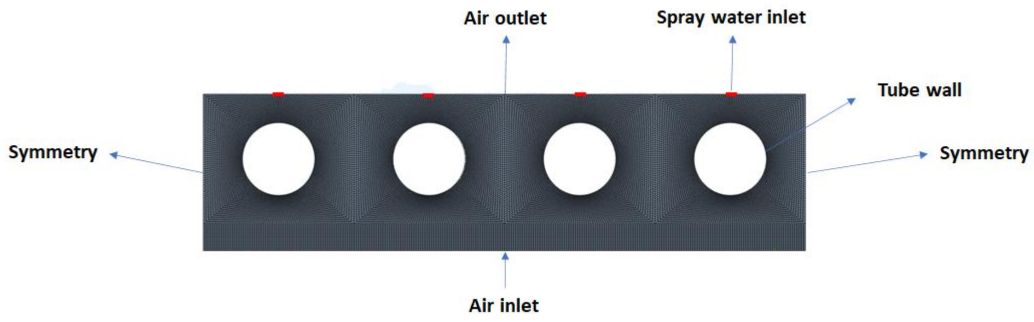

Figure 2.6 : Boundary conditions of CFD mixture model.

The pressure-velocity coupling was handled using the Coupled algorithm for improved stability in multiphase simulations. Various air inlet velocities were tested (0.01 m/s, 0.5 m/s, 1 m/s, and 1.5 m/s) while maintaining a constant water inlet velocity of 1 m/s. The boundary and initial conditions, including inlet air temperature and humidity, were assigned based on the values obtained during the experimental described in Section 2.1.

During the experiments, the inlet and outlet air temperatures, along with the water temperatures, were recorded. These experimental results were then utilized to validate the boundary conditions applied in the numerical model.

To provide a theoretical foundation for the CFD model, the fundamental governing equations describing mass, momentum, energy, and species transport in the air-water system are expressed as follows:

- Continuity Equation:

$$\frac{\partial \rho_m}{\partial t} + \nabla \cdot ((\rho_m \vec{v}_m) = 0 \qquad (2.13)$$

where $\rho_m = \sum_k^2 \alpha_k \rho_k$ is the mixture density, α_k is the volume fraction of phase k, and $\vec{v}_m$ is the mass-averaged mixture velocity. Air-vapor mixture was selected as the primary phase (k = 1), and liquid water was defined as the secondary phase (k = 2).

Table 2.8 : Summary of CFD mixture model setup.

Discretization scheme	First order upwind
Time	Transient
Turbulence model	k-omega (SST)
Multiphase model	Mixture
Drag Coefficient	Schiller-naumann
Evaporation Mechanism	Lee Model
Volume Faction Cutoff	$1\ x\ 10^{-6}$
Interface Model	Sharp/Dispersed
Slip Velocity	Manninen-et-al
Surface Tension Coefficient (N/m)	0.072
Gravitational acceleration (m/s²)	-9.81
Atmospheric Pressure (Pa)	99,5

- Momentum equation:

$$\frac{\partial(\rho_m \vec{v}_m)}{\partial t} + \nabla \cdot (\rho_m \vec{v}_m \vec{v}_m) = -\nabla p + \nabla \cdot \left(\mu_m (\vec{v}_m + \vec{v}_m^T)\right) + \rho_m \vec{g} + \vec{F} \qquad (2.14)$$

Here, μ_m is the effective viscosity of the mixture, and $\vec{F}$ includes interfacial and external body forces.

Table 2.9 : Summary of CFD mixture model boundary conditions.

Name	Data
Air Inlet (m/s)	0.01 – 1.5
Air Temperature (°C)	29.0
Specific Humidity (kg/kg vapor)	1.09×10^{-2}
Spray Water velocity (m/s)	1
Spray Water Temperature (°C)	24.7
Tube Wall Temperature (°C)	30.4

- Volume Fraction Equation (Secondary Phase k):

$$\frac{\partial \alpha_k}{\partial t} + \nabla \cdot (\alpha_k \vec{v}_m) + \nabla \cdot (\alpha_k \vec{v}_{dr,k}) = 0 \tag{2.15}$$

where $\vec{v}_{dr,k} = \vec{v}_{mk} - \vec{v}_m$ is the drift velocity of phase k relative to the mixture.

- Energy equation:

$$\frac{\partial (\rho_m h_m)}{\partial t} + \nabla \cdot (\rho_m \vec{v}_m\, h_m) = \nabla \cdot (k_{\text{eff}} \nabla T) \tag{2.16}$$

where h_m is the mixture enthalpy and k_{eff} is the effective thermal conductivity.

- Species Transport Model:

$$\frac{\partial (\rho_m Y_i)}{\partial t} + \nabla \cdot (\rho_m \vec{v}_m\, Y_i) = \nabla \cdot (\rho_m D_{i,m} \nabla Y_i) \tag{2.17}$$

where Y_i is the mass fraction of species *i* and $D_{i,m}$ is the diffusion coefficient of species *i* in the mixture.

- Lee Evaporation Model:

$$\dot{m} = C \cdot \rho_l \cdot \frac{T - T_{\text{sat}}}{T_{\text{sat}}} \tag{2.18}$$

where C is the empirical mass transfer coefficient, ρ_l is density of liquid phase, T is local temperature and T_{sat} is the saturation of water.

User-Defined Function was implemented to dynamically compute the saturation temperature T_{sat} based on the local partial pressure of water vapor. Function evaluates the volume fraction of the liquid and vapor phases, along with their respective mass fractions, to determine the water vapor partial pressure p_{wv}. This value is then used in the inverted form of the Tetens equation to calculate the corresponding saturation temperature in Kelvin. The implemented logic is as follows:

(1) If the cell is fully occupied by liquid water (i.e., volume fraction =1), the total local pressure (static + operating) is used directly as the water vapor pressure.

(2) Otherwise, the partial pressure is calculated from the local mixture pressure and molar fractions of water vapor and dry air.

(3) For very low vapor concentrations $Y_{wv} < 0.01$, a simplified linear relation is used to avoid numerical instability.

(4) The general expression used for most cases is:

$$T_{\text{sat}} = \frac{4947.46 - 82.46 \ \cdot \log_{10}(p_{wv})}{23.69 - 2.3 \ \cdot \log_{10}(p_{wv})} \tag{2.19}$$

where T_{sat} is in Kelvin and p_{wv} in Pa.

This approach allows evaporation to occur below the classical saturation temperature, enabling the model to simulate realistic evaporation and humidification effects in the airflow. The UDF was integrated into the mass transfer source terms of the Lee model in ANSYS Fluent.

2.3.2 2D discrete phase model CFD simulation setup

The system involves complex interactions between a continuous gas phase (moist air) and a dispersed liquid phase (water droplets). Given that the volume fraction of the liquid water spray is significantly low (<10%), the Euler-Lagrange approach is adopted as the most suitable and computationally efficient method.

The 2D computational domain represents a vertical cross-section of the cooling tower, including the serpentine heat exchanger tubes and was discretized using a fully structured quadrilateral mesh consisting of over 160,000 elements, provided in Figure 2.7. In contrast to the geometry employed in the multiphase mixture model, the present setup incorporates a complete 10-row serpentine tube arrangement, including the spray zone at the top and the raining zone at the bottom. To ensure a physically accurate representation of the counter-flow configuration, the boundary conditions were illustrated in Figure 2.8.

In this framework, the continuous phase (air and water vapor mixture) is treated as a continuum and is described by the Navier-Stokes equations solved on an Eulerian grid. The dispersed phase (water droplets), conversely, is tracked through the calculated flow field in a Lagrangian frame. This approach, implemented in the commercial CFD software ANSYS Fluent, allows for a detailed analysis of droplet trajectories, heat transfer, and phase change). The interaction between the phases is modeled using the Discrete Phase Model. A transient simulation approach was selected.

The continuous phase is a mixture of air and water vapor, treated as an ideal gas. The flow is considered transient, turbulent, and incompressible. The governing equations for mass, momentum, energy, and species transport are solved. For this study, the Shear-Stress Transport k-ω model was selected. This model is renowned for its robustness and accuracy in handling wall-bounded flows, adverse pressure gradients, and flow separation, which are all present in the flow around the serpentine tubes. The SST k-ω model effectively blends the robust and accurate formulation of the k-ω model in the near-wall region with the free-stream independence of the k-ε model in the far field.

The energy equation was enabled to solve for the temperature distribution throughout the domain. Crucially, the "Diffusion Energy Source" option was activated within the species transport model. This term accounts for the enthalpy transport due to the diffusion of different species (i.e., water vapor diffusing into the air), which is a critical component of the energy balance in an evaporative cooling process.

The transport and mixing of water vapor within the air are modeled by solving a species transport equation for the mass fraction of H_2O. The liquid water spray is modeled using the Discrete Phase Model. The trajectories of individual water droplets are computed by integrating the force balance on the particle in a Lagrangian reference frame.

To provide a theoretical foundation for the CFD model, the fundamental governing equations describing mass, momentum, energy, and species transport in the air-water system are expressed as follows:

- Continuity Equation:

$$\frac{\partial \rho}{\partial t} + \nabla \cdot (\rho \vec{v}\,) = 0 \qquad (2.20)$$

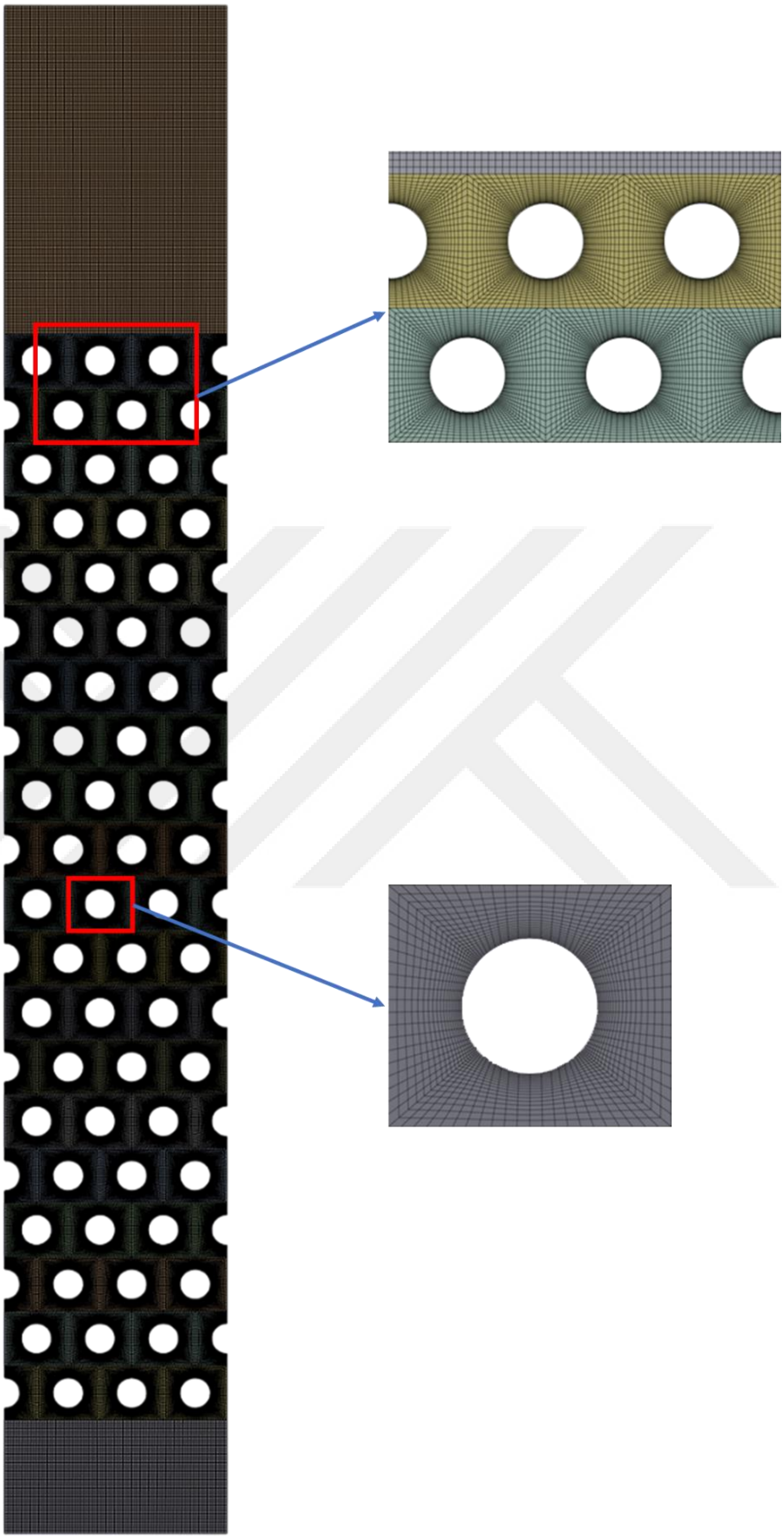

Figure 2.7 : The mesh structure of 2D DPM model generated by Ansys Fluent.

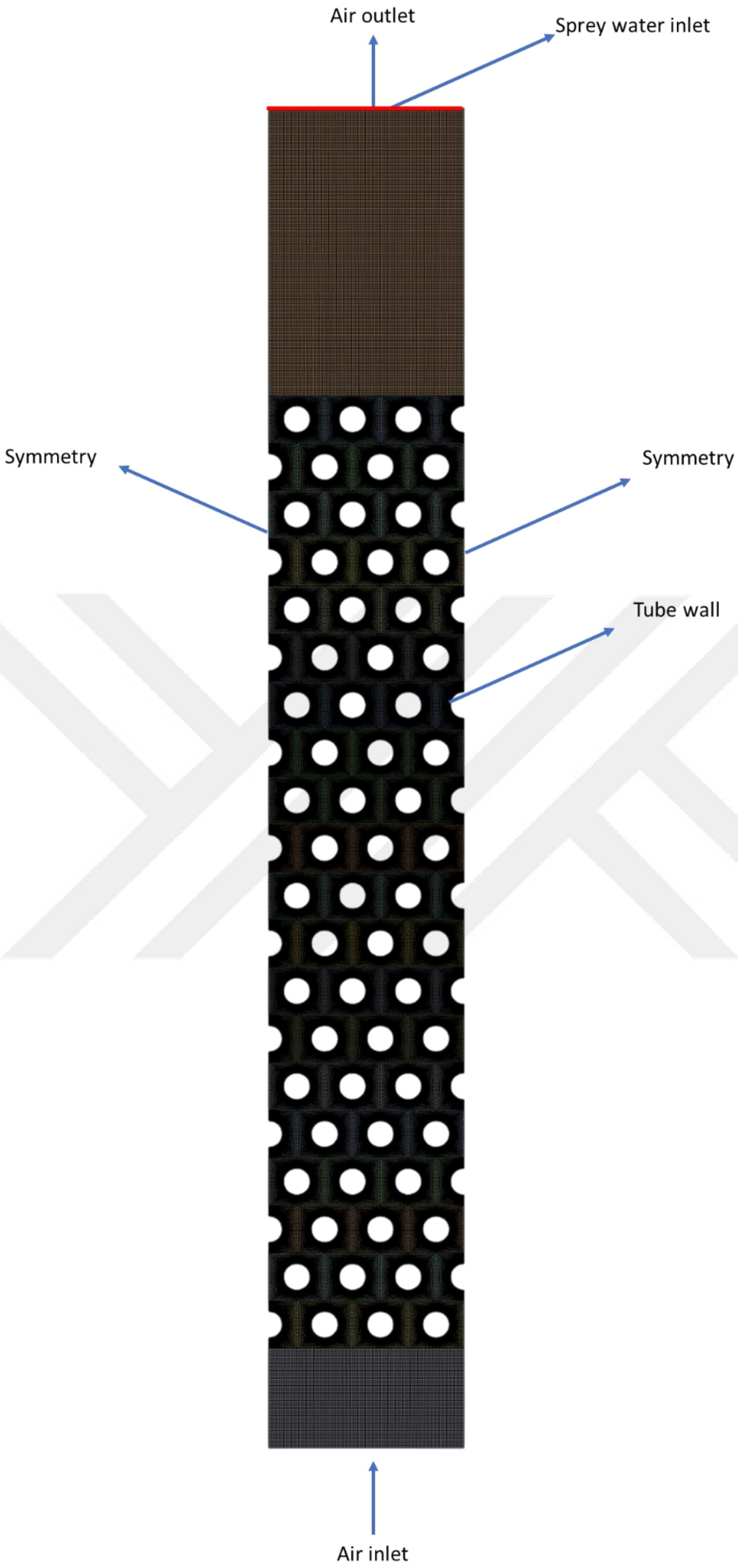

Figure 2.8 : Boundary conditions of CFD DPM model.

- Momentum equation:

$$\frac{\partial(\rho\vec{v}\,)}{\partial t} + \nabla\cdot(\rho\vec{v}\vec{v}\,) = -\nabla p + \nabla\cdot\left(\mu\left(\vec{v}+\overline{v^{T}}\right)\right) + \rho\vec{g} + \vec{F} \tag{2.21}$$

- Energy equation:

$$\frac{\partial(\rho h)}{\partial t} + \nabla\cdot(\rho\vec{v}h) = \nabla\cdot(k_{\text{eff}}\nabla T) \tag{2.22}$$

- Species Transport Model:

$$\frac{\partial(\rho Y_i)}{\partial t} + \nabla\cdot(\rho\vec{v}\,Y_i) = \nabla\cdot(\rho D_i \nabla Y_i) \tag{2.23}$$

The SST k-ω turbulence model is given as follows:

- Turbulent kinetic energy κ:

$$\frac{\partial(\rho\kappa)}{\partial t} + \nabla\cdot(\rho u\kappa) = \nabla\cdot\left[\left(\mu+\frac{\mu_t}{\sigma_\kappa}\right)\nabla\kappa\right] + G_\kappa + G_b + Y_k \tag{2.24}$$

- Spesific dissipation rate ω:

$$\frac{\partial(\rho\omega)}{\partial t} + \nabla\cdot(\rho u\omega) = \nabla\cdot\left[\left(\mu+\frac{\mu_t}{\sigma_\kappa}\right)\nabla\omega\right] + G_\omega + G_{\omega b} + D_w - Y_\omega \tag{2.25}$$

where G_κ represents the generation of turbulence kinetic energy due to the mean velocity gradients, G_ω represents the generation of ω, G_b is the generation of turbulence kinetic energy due to buoyancy, σ_κ and σ_ω are the turbulent Prandtl numbers for κ and ω, Y_k and Y_ω are represent the dissipation of κ and ω due to turbulance, D_w represents the cross-diffusion term.

The balance between the particle's inertia and the acting forces can be represented as:

$$m_{pt}\frac{d\vec{u}_{pt}}{dt} = \frac{m_{pt}(\vec{u}-\vec{u}_{pt})}{\tau_r} + m_{pt}\frac{\vec{g}(\vec{\rho}_{pt}-\vec{\rho})}{\rho_{pt}} + \vec{F} \tag{2.26}$$

where m_{pt} is the particle mass, density, $\vec{u}$ is the fluid phase velocity, ρ_{pt} is the density of the particle, $\vec{F}$ is an additional force, and τ_r is the particle relaxation time calculated as:

$$\tau_r = \frac{4\rho_{pt}d_{pt}^2}{3\mu C_d \text{Re}} \tag{2.27}$$

where C_d is drag coefficient d_{pt} is the particle diameter, and Re is the relative Reynolds number, which is defined as:

$$\mathrm{Re} = \frac{\rho d_{pt}\left|\vec{u}_{pt} - \vec{u}\right|}{\mu} \tag{2.28}$$

A critical aspect of this simulation is the two-way coupling established between the discrete and continuous phases, which was enabled via the "Interaction with Continuous Phase" option. This setting is fundamental to the physical realism of the model, as it ensures a reciprocal influence between the phases. The continuous phase governs droplet trajectories through drag and turbulent dispersion, while the droplets, in turn, modify the continuous phase by exchanging momentum, heat, and mass. This two-way exchange is the primary mechanism driving the evaporative cooling and humidification of the air.

To accurately capture the droplets' response to the evolving flow field in this transient simulation, an unsteady particle tracking scheme was employed. This method synchronizes the advancement of particle positions with the continuous phase flow time. For computational efficiency and to prevent solver divergence from erratic trajectories, a maximum of 1000 integration steps was allocated for each particle stream. Furthermore, "High-Resolution Tracking" was enabled to enhance the precision of trajectory calculations, especially near complex geometries and boundaries.

Water droplets, defined with the material properties of water-liquid, were introduced into the domain from the top boundary using a Surface Injection. The water droplet diameter was set to 2 mm to investigate its effect on evaporation and film formation. A total mass flow rate of 0.85 kg/s was distributed uniformly across this injection surface. To realistically simulate the atomization process where a liquid jet disintegrates into smaller droplets, the Breakup model was activated. This model dynamically simulates the secondary breakup of droplets due to aerodynamic forces, leading to a more physically representative droplet size distribution throughout the cooling tower.

The physical processes governing droplet behavior were meticulously defined. The phase change from liquid to water vapor was modeled by specifying H_2O as the evaporating species. The accompanying heat transfer calculations accounted for the temperature-dependent latent heat of vaporization, ensuring that the energy exchange during evaporation was accurately modeled based on the local droplet temperature. Finally, a gravitational acceleration was applied in the vertical direction, influencing both the air flow and the droplet trajectories. Detailed information about the model setup is provided in Table 2.10. The data related to the boundary conditions is shown in Table 2.11.

For the serpentine tube walls, the DPM boundary condition was set to wall-film. This sophisticated model allows droplets that impinge on the tube surfaces to form a thin liquid film instead of reflecting or being trapped. This film is then subject to the full heat and mass transfer physics: it is heated by the hot tube wall and evaporates into the surrounding air stream. In addition, the initial wall film thickness was set to 1 mm to assess its influence on heat and mass transfer behavior. The reason why the water droplet diameter and spray film thickness are treated as variable parameters is that they were not measured in the experiment; instead, suitable parameter ranges were selected in accordance with previous studies [8].

The SIMPLE (Semi-Implicit Method for Pressure Linked Equations) algorithm was used for pressure-velocity coupling. To ensure high accuracy, a Second Order Upwind scheme was employed for the spatial discretization of the momentum, turbulent kinetic energy (k), specific dissipation rate (ω), species (H_2O), and energy equations. A First Order Implicit scheme was used for the transient formulation. A fixed time step size (Δt) of 2×10^{-5} was chosen. This small time step ensures numerical stability and accurately resolves the temporal evolution of both the flow field and the particle trajectories.

Within each time step, the solution was iterated until the scaled residuals for all solved equations dropped below 10^{-4}, with the energy and species residuals monitored to a stricter criterion of 10^{-6}.

The transient simulation was run not for a fixed duration but until the system reached a quasi-steady state. This state was identified by monitoring the mass-flow averaged specific humidity at the interior. The simulation was considered fully converged and was terminated when this value ceased to show any significant secular change and oscillated around a constant mean. This approach ensures that the results represent the stable operating condition of the cooling tower.

Table 2.10 : Summary of CFD DPM model setup.

Discretization scheme	Second order upwind
Time	Transient
Turbulence model	k-omega (SST)
Injection Type	Surface
Particle Type	Droplet
Discrete Phase Boundary Condition Type	Wall Film
Impingement/Splashing Model	Stanton-Rutland
Gravitational acceleration (m/s²)	-9.81
Atmospheric Pressure (Pa)	99,505

Table 2.11 : Summary of CFD DPM 2D model boundary conditions.

Name	Data
Air Inlet (m/s)	3.5
Air Temperature (°C)	29.0
Specific Humidity (kg/kg vapor)	1.09×10^{-2}
Injection Diameter (mm)	2
Wall Film Initial Height (mm)	1
Spray Water Total Mass Flow Rate (kg/s)	0.85
Spray Water Temperature (°C)	24.7
Tube Wall Temperature (°C)	30.4

2.3.3 3D discrete phase model CFD simulation setup

To complement the 2D analysis, a fully three-dimensional CFD model was developed. The 3D computational domain was generated by extruding the previously defined 2D cross-section by 60 mm in the spanwise direction, thereby constructing a realistic representation of the cooling tower volume. Apart from this geometric extension, all physical models, boundary conditions, and numerical schemes described in Section 2.3.2 were retained to ensure consistency and comparability between the 2D and 3D simulations.

The resulting domain was discretized with a fully structured hexahedral mesh, as shown in Figure 2.9, with grid refinement applied near the serpentine tube walls and the spray region to better resolve droplet–film interactions. The total number of elements exceeded $2.5\ x\ 10^6$, ensuring adequate spatial resolution for capturing the complex three-dimensional flow structures.

As in the 2D case, the moist air was treated as the continuous Eulerian phase, governed by the Navier–Stokes, energy, and species transport equations, while water droplets were tracked in a Lagrangian framework using the Discrete Phase Model. Two-way coupling between phases, transient particle tracking, droplet breakup, evaporation, and film formation on the serpentine tubes were all enabled identically to the 2D setup. The same turbulence model (SST k-ω) and discretization schemes were employed.

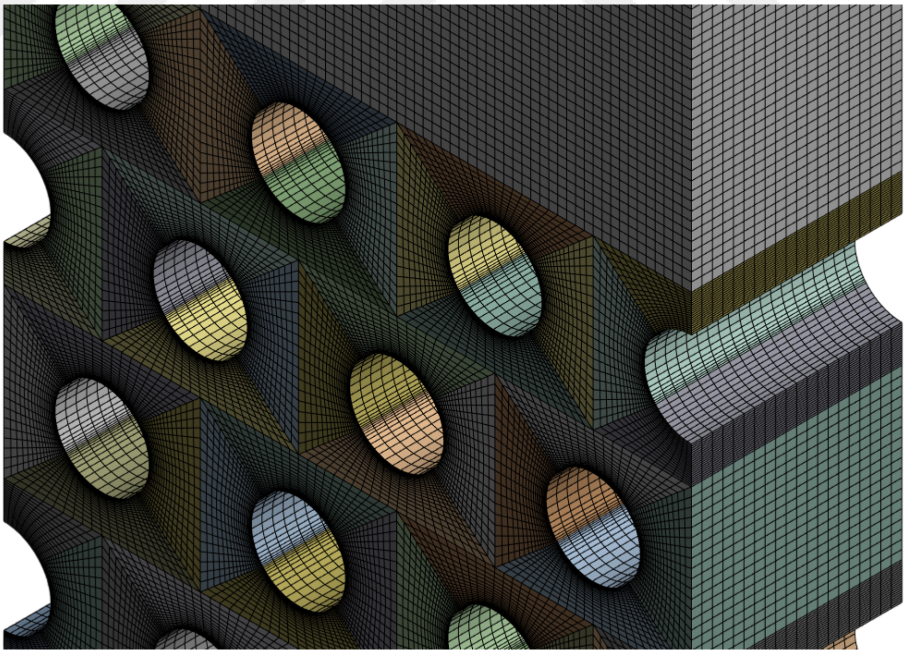

Figure 2.9 : The mesh structure of 3D DPM model generated by Ansys Fluent.

Boundary conditions for the inlet air, spray water injection, and tube wall temperature followed the values summarized in Table 2.12, corresponding to the 3D configuration. The only modification was the increased domain depth, which resulted in a proportionally different spray injection surface and correspondingly distributed droplet mass flow rate.

Table 2.12 : Summary of CFD DPM 3D model boundary conditions.

Name	Data
Air Inlet (m/s)	3.5
Air Temperature (°C)	29.0
Specific Humidity (kg/kg vapor)	1.09×10^{-2}
Injection Diameter (mm)	2
Wall Film Initial Height (mm)	1
Spray Water Total Mass Flow Rate (kg/s)	0.175
Spray Water Temperature (°C)	24.7
Tube Wall Temperature (°C)	30.4

The SIMPLE pressure–velocity coupling algorithm and second-order upwind spatial discretization were again adopted, with a fixed time step of $\Delta t = 2 \times 10^{-5}$ s. Convergence was monitored by tracking the residuals and the evolution of domain-averaged humidity, and the simulation was terminated once a quasi-steady operating condition was achieved.

2.4 Mesh Independence and Validation

2.4.1 Mixture multiphase model CFD validation

To ensure the reliability and accuracy of the numerical results, a mesh independence study was conducted prior to the final simulations. Three different mesh densities were tested: coarse (≈35,000 cells), medium (≈50,000 cells), and fine (≈98,000 cells), each generated using a structured quadrilateral topology to preserve geometric fidelity around the coil surfaces and spray interaction zones. The key parameters assessed for mesh independence included wall heat flux, water film temperature and flow distribution. The results showed negligible variation (<5%) between the medium and fine meshes, indicating sufficient spatial resolution at the medium mesh level, as shown in Figure 2.10. Therefore, the medium mesh containing approximately 50,000 elements was adopted for all subsequent simulations to balance computational cost and accuracy.

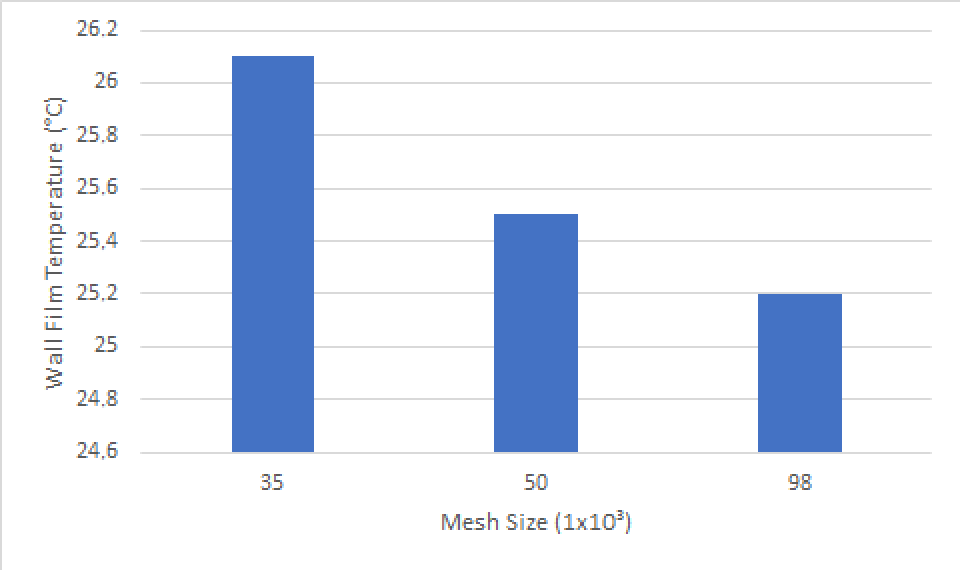

Figure 2.10 : The mean value of wall film temperatures under mixture model mesh sizes.

2.4.2 Discrete phase model CFD validation

Similarly, to ensure the reliability and accuracy of the numerical results, a mesh independence study was conducted prior to the final simulations. Three different mesh densities were tested: coarse (≈128,000 cells), medium (≈160,000 cells), and fine (≈315,000 cells), each generated using a structured quadrilateral topology to preserve geometric fidelity around the coil surfaces and spray interaction zones. The key parameters assessed for mesh independence included air-side outlet temperature, wall heat flux, relative humidity, and water film temperature distribution. The results showed negligible variation (<5%) between the medium and fine meshes, indicating sufficient spatial resolution at the medium mesh level. Therefore, the medium mesh containing approximately 160,000 elements was adopted for all subsequent simulations to balance computational cost and accuracy.

The outlet air humidity between simulation and experimental values was within acceptable limits, with a maximum deviation of less than 8%, thereby confirming that the CFD model could accurately capture the coupled heat and mass transfer behavior occurring within the closed-circuit cooling tower. The effect of coarse, medium, and fine mesh resolutions on the outlet air humidity is presented in Table 2.13.

Table 2.13 : The mean value of outlet air humidifies under DPM model mesh sizes.

Name	Outlet Air Humidity
Coarse (≈128,000 cells)	1.26×10^{-2}
Medium (≈160,000 cells)	1.25×10^{-2}
Fine (≈315,000 cells)	1.25×10^{-2}

3. RESULTS AND DATA ANALYSIS

3.1 Experimental Results

A series of full-scale field experiments were conducted to evaluate the thermal performance of the closed-circuit cooling tower under realistic ambient conditions. During the experimental campaign, the dry-bulb and wet-bulb temperatures of the inlet air were recorded as 29.0 °C and 19.7 °C, respectively. The process water entered the system at 34.9 °C and was cooled to 25.9 °C at the outlet, indicating a total temperature reduction of 8.98 °C. To ensure measurement reliability, all data were averaged over a one-hour period under steady-state conditions.

Using the collected measurements, two important performance indicators—range and approach—were calculated. The range, defined as the temperature difference between the inlet and outlet water, was found to be 6.97 °C, while the approach, the difference between the outlet water temperature and the ambient wet-bulb temperature, was 6.17 °C. These values provide insight into the cooling efficiency of the tower and are illustrated in Figure 3.1.

Based on empirical thermal resistance formulations and the known flow and temperature characteristics, the spray heat transfer coefficient was determined to be approximately 1163 $W/m^2 \cdot K$. Additionally, the total evaporation loss observed during the experimental run was measured to be 0.54 m^3/h, which represents a significant contribution to the heat rejection mechanism of the tower under hot and humid conditions.

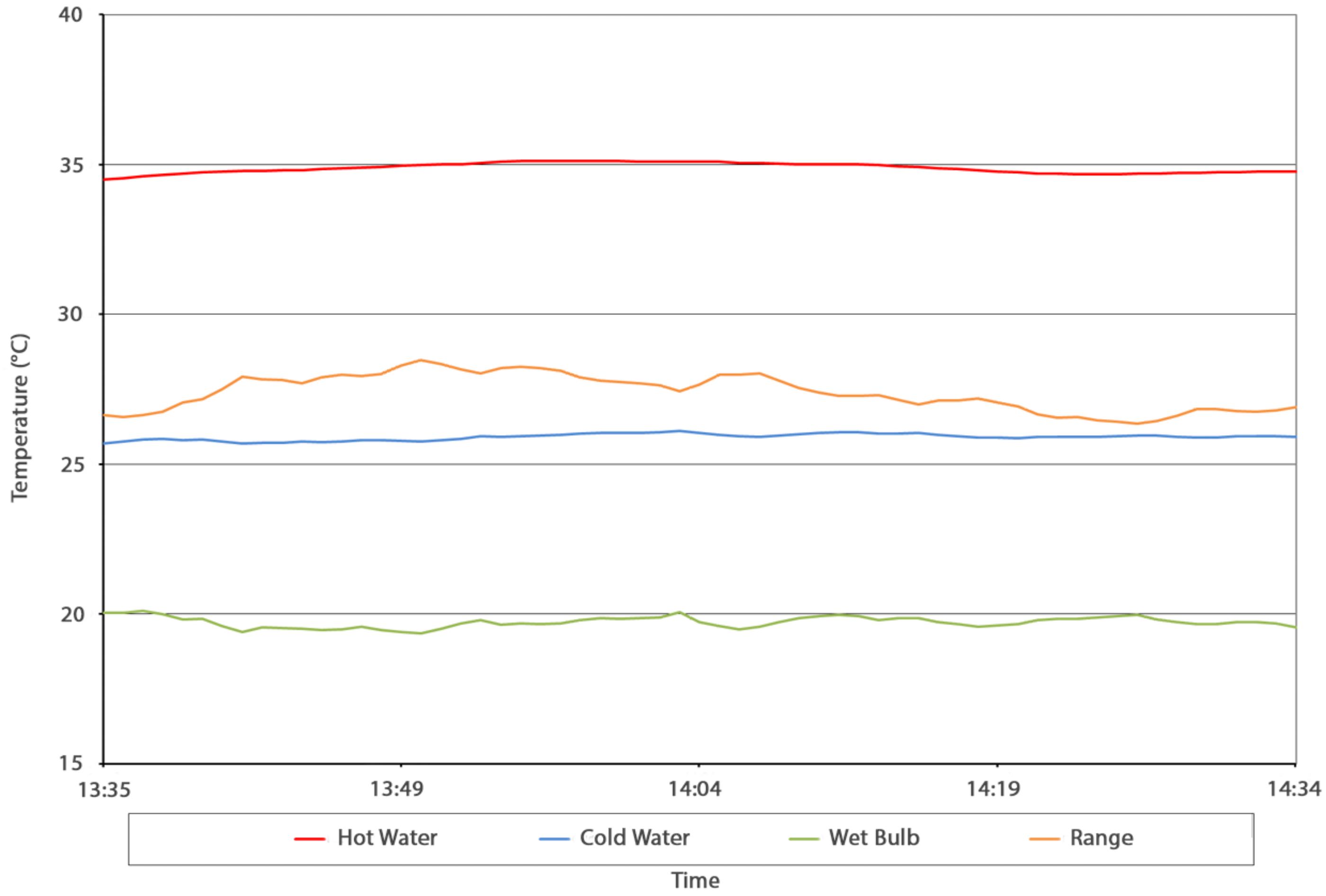

Figure 3.1 : Variation of hot water, cold water, wet bulb temperature, and range over a 1-hour period in the cooling tower.

3.2 CFD Simulation Results

3.2.1 Mixture model CFD simulation results

To complement and validate the experimental findings, a numerical model was developed to simulate the coupled heat and mass transfer processes occurring within the CCCT. The air velocity, a critical parameter in the simulation, was varied from 0 to 1.5 m/s at the tower's widest cross-section. Due to geometric contraction in narrower sections, local air velocities increased accordingly. As the air velocity increased, several important physical phenomena were observed.

At higher air velocities, the water film became noticeably thinner, especially at the bottom of the coil tubes, due to increased shear stress exerted by the airflow. Concurrently, the spray film heat transfer coefficient, the outlet air specific humidity, and the mean mass transfer rate all showed upward trends. These relationships are illustrated in Figures 3.2, 3.3, and 3.4, respectively.

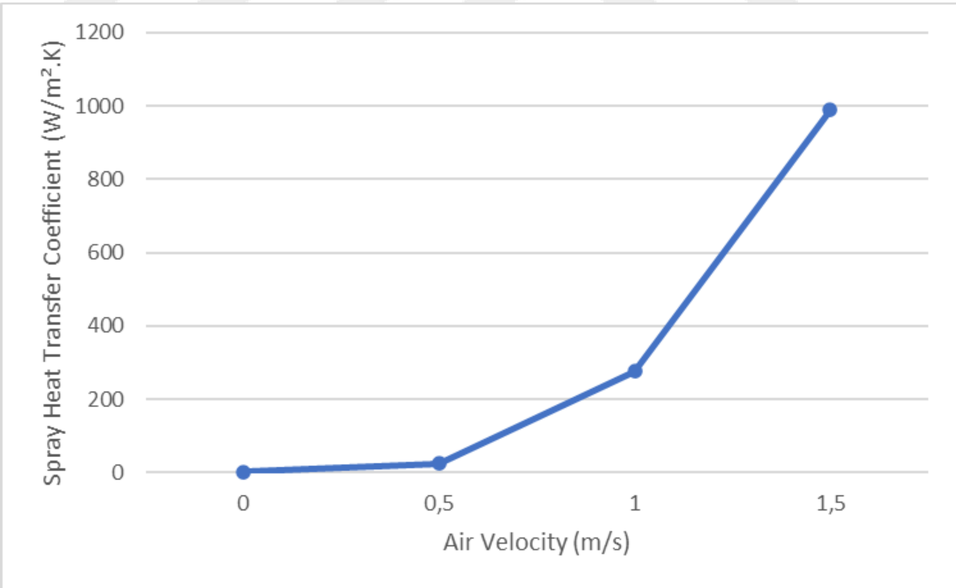

Figure 3.2 : Variation of heat transfer coefficient with air velocity.

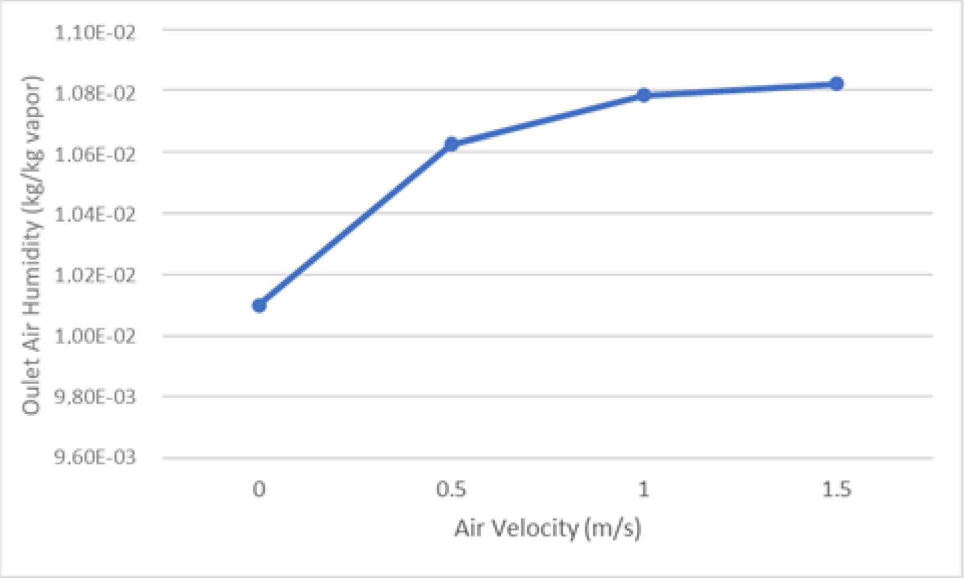

Figure 3.3 : Variation of outlet air humidity with air velocity.

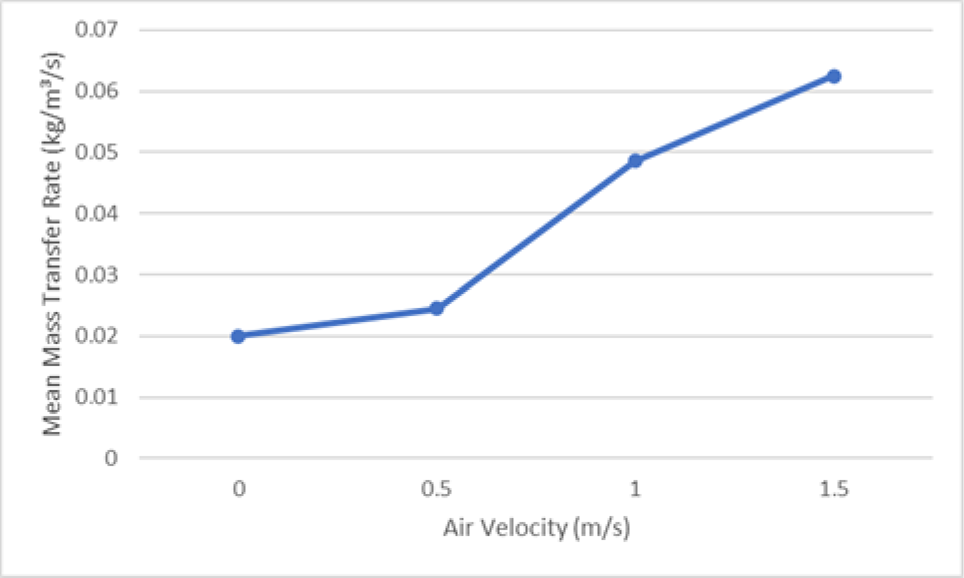

Figure 3.4 : Variation of mean heat transfer rate with air velocity.

Specifically, at an air velocity of 1.5 m/s, the outlet air specific humidity predicted by the simulation was 1.08×10^{-2} kg/kg vapor. The spatial distributions of temperature, specific humidity, and mass transfer rate for various air velocities are presented in Figures 3.5, 3.6, and 3.7, respectively.

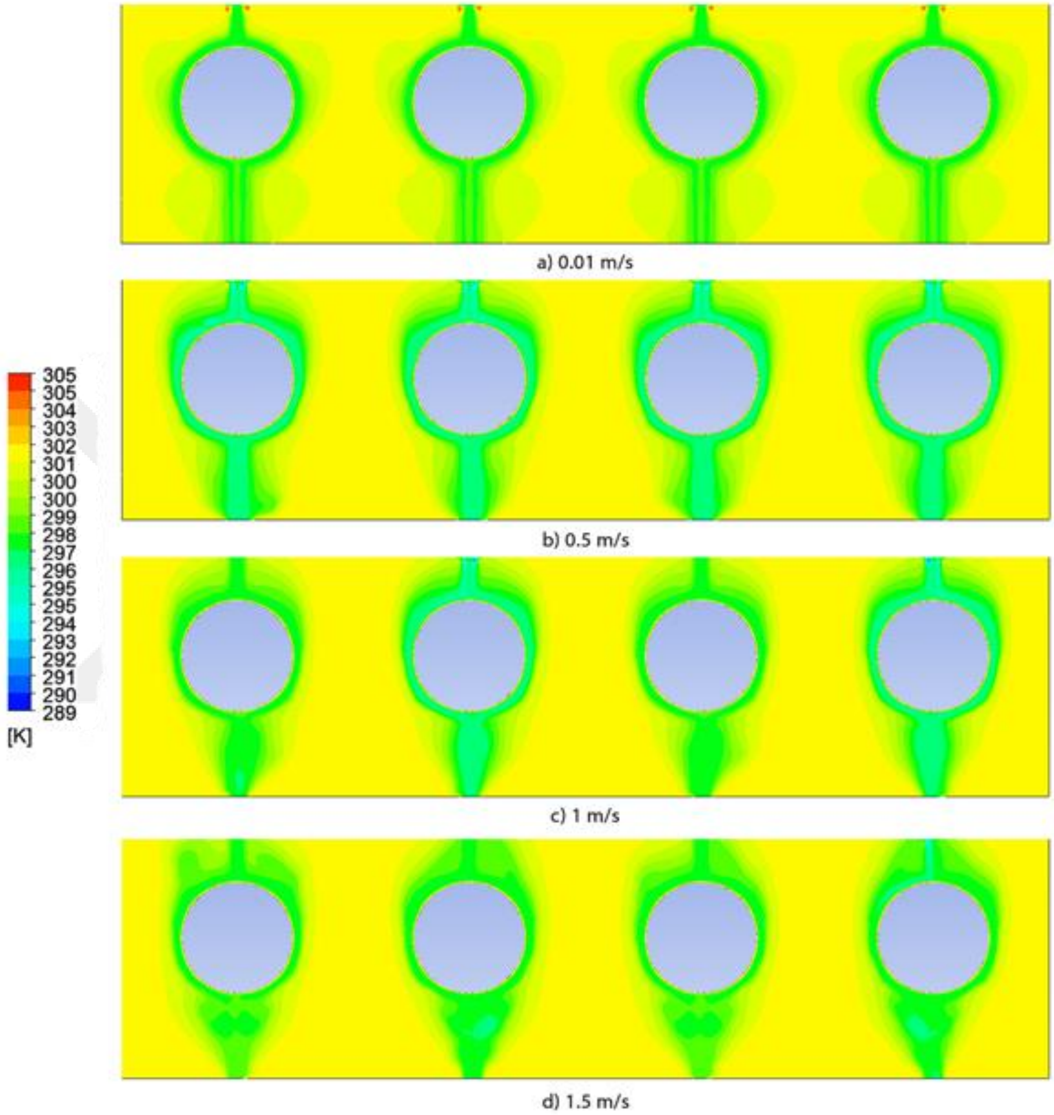

Figure 3.5 : Temperature contours around the serpentine tubes depending on the air velocity.

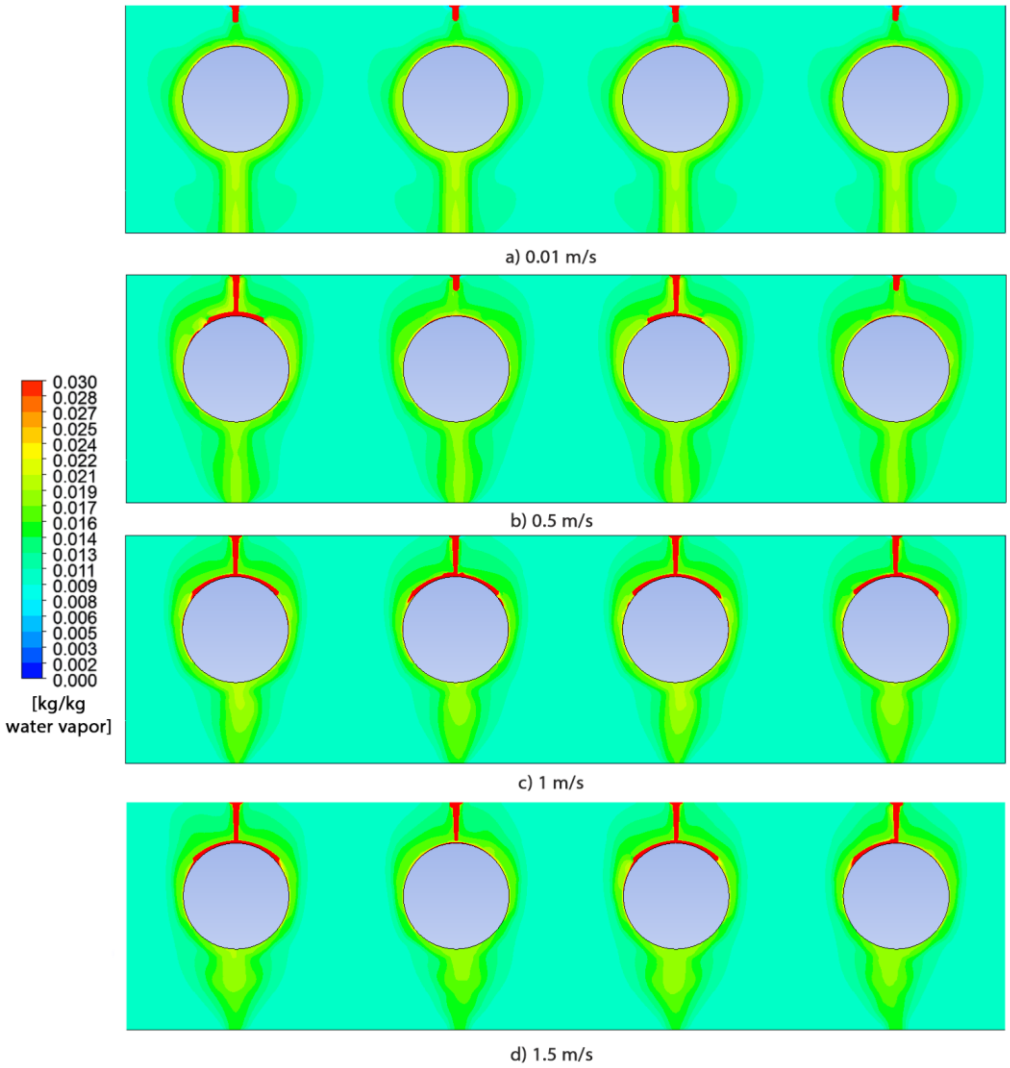

Figure 3.6 : Mass fraction of water vapor contours around the serpentine tubes depending on the air velocity.

Furthermore, based on simulated thermal and flow fields, the spray heat transfer coefficient was calculated to be approximately 1000 W/m²·K, which is significantly higher than the expected value. Unfortunately, due to the presence of spray in the experiment and the limitations of the mixture multiphase model, the sharp/dispersed interphase approach—implemented through an orifice-shaped inlet—tended to overpredict the water film thickness and velocity on the serpentine tubes. This likely resulted in an overestimation of the heat transfer coefficient. Therefore, it was decided to proceed with the DPM approach for further simulations.

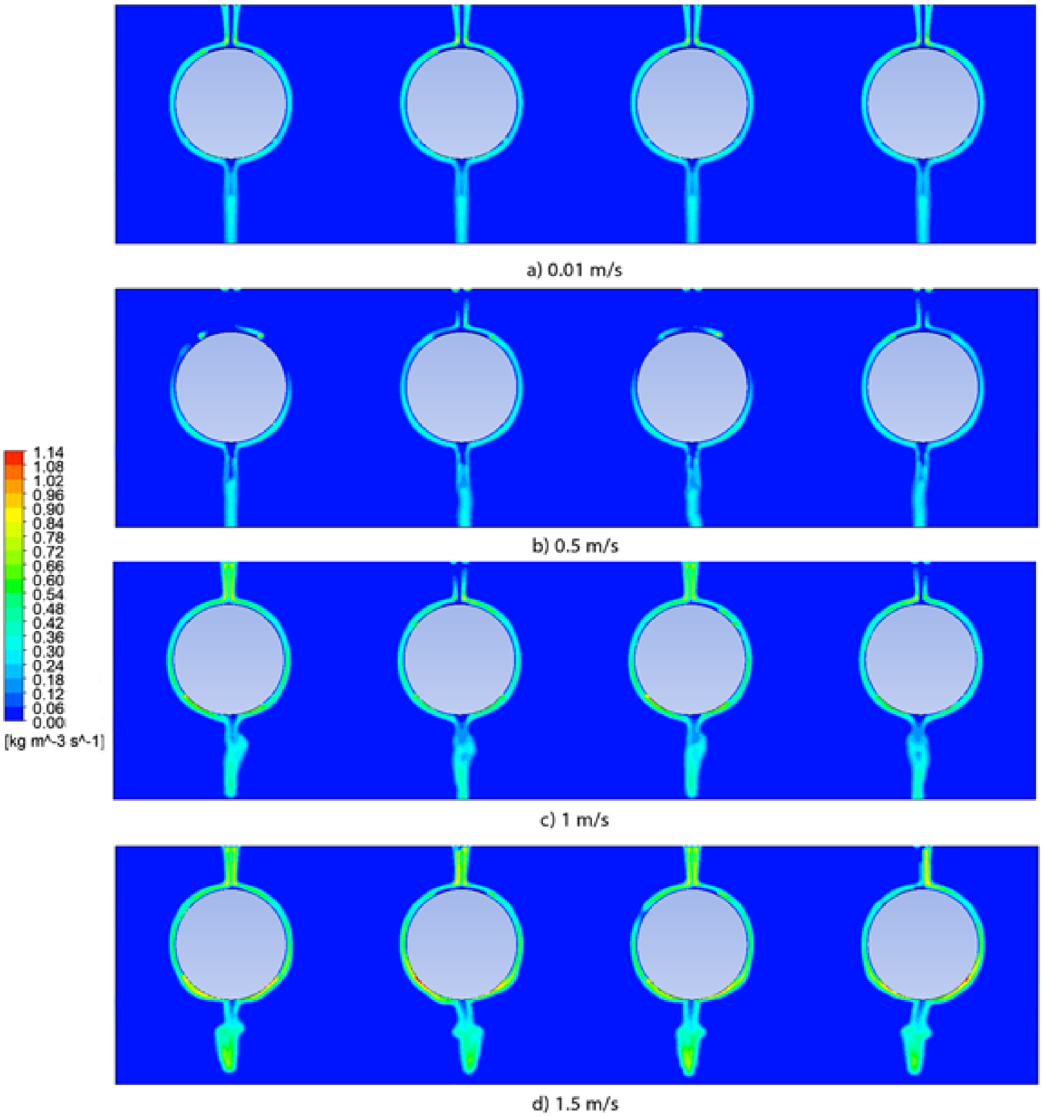

Figure 3.7 : Mass transfer rate contours around the serpentine tubes depending on the air velocity.

3.2.2 2D discrete phase model CFD simulation results

The provided image, Figure 3.8, presents the instantaneous velocity magnitude contours from a 2D transient simulation of fluid flow across a staggered tube bank, which represents the serpentine coils within a cooling tower, captured at a time of 1 s. The velocity field, ranging from 0 m/s to approximately 16.0 m/s reveals a highly complex and unsteady flow pattern characteristic of flow over bluff bodies. Furthermore, Figure 3.9 and 3.10 illustrates the corresponding streamlines and pathlines, providing additional insight into the flow behavior.

The highest fluid velocities are observed in the gaps between the tubes, a result of the flow accelerating through the reduced cross-sectional area. The dark blue color on the tube surfaces correctly illustrates the no-slip boundary condition, where the fluid velocity is zero. The unsteady nature of air flow generates high levels of turbulence. This turbulence, while causing a pressure drop, is the primary mechanism for disrupting the thermal boundary layer and promoting efficient heat and mass transfer between the continuous phase (air) and the tube surfaces, which is the essential function of the serpentine coils in a cooling tower.

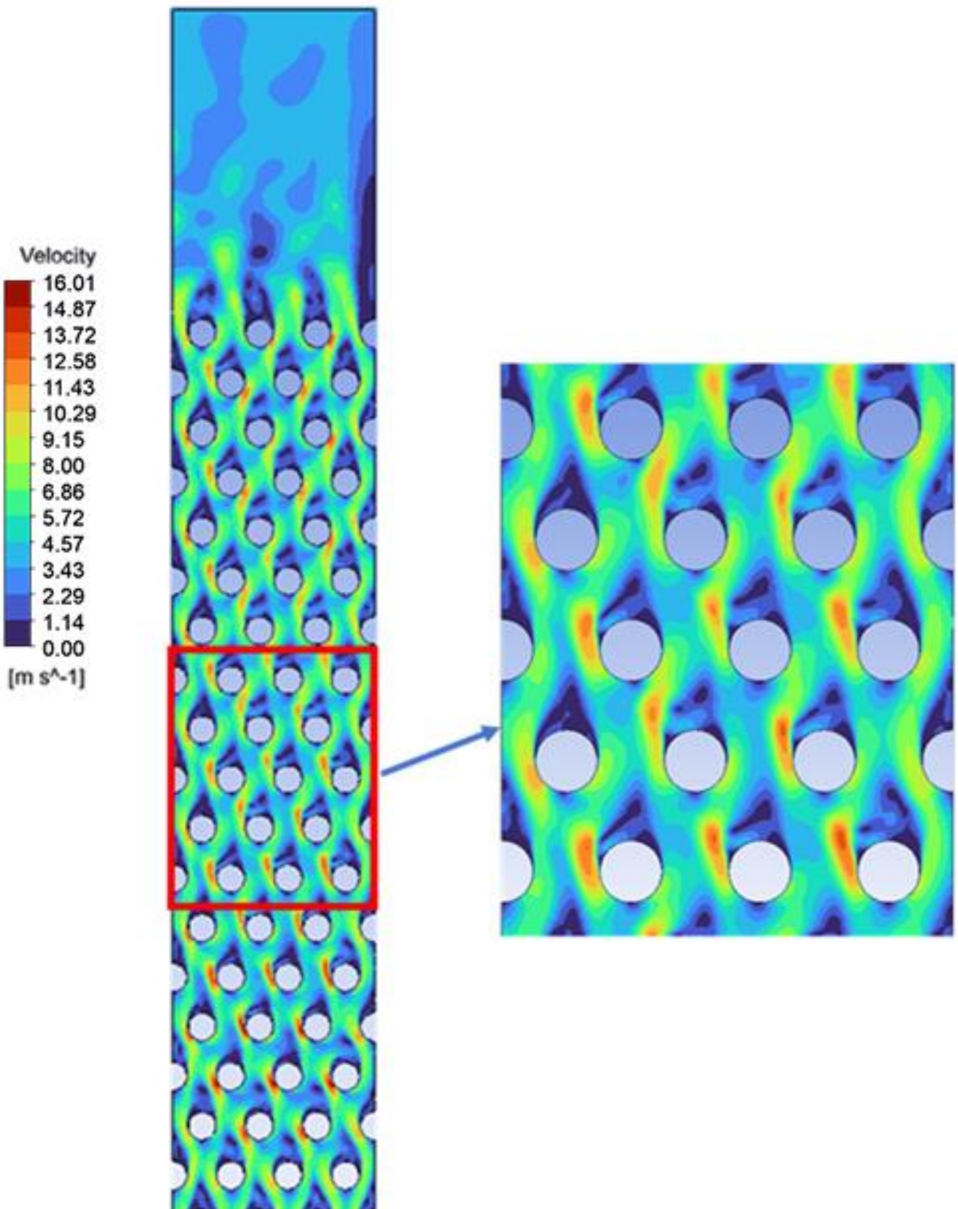

Figure 3.8 : Velocity contours around the serpentine tubes**.**

Figure 3.11 illustrates the contours of the water vapor (H_2O) mass fraction, providing critical insight into the evaporative mass transfer process within the serpentine coil section at the same transient instant. The color map represents the mass fraction of water vapor in the air, ranging from 0.011 representing drier air at the inlet to a maximum of 0.016 more humid air.

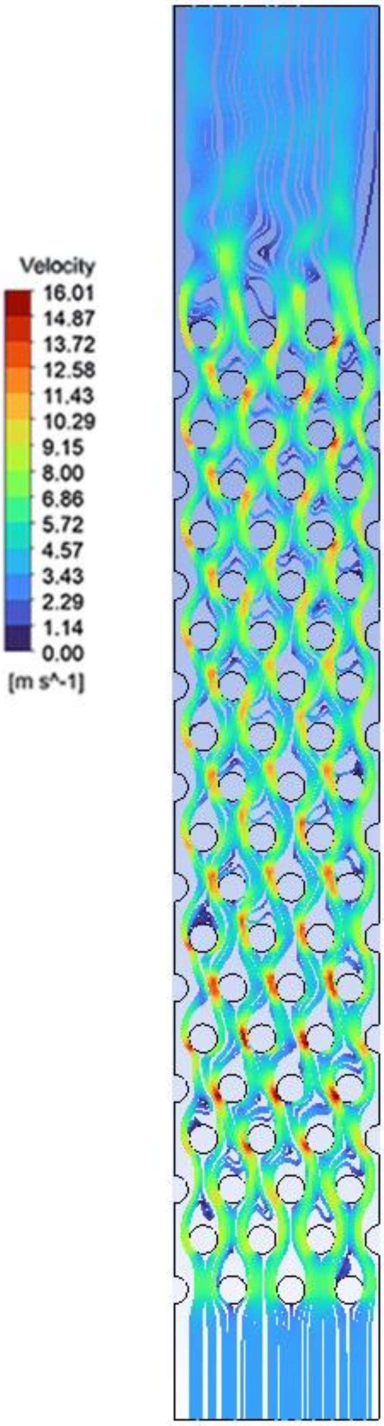

Figure 3.9 : Streamlines around the serpentine tubes.

The air enters the domain from the bottom with a baseline H_2O mass fraction of 1.09×10^{-2}. As the air flows upwards across the successive rows of tubes, it progressively entrains more moisture. This is visualized by the gradual color change from dark blue at the inlet to light blue and then cyan towards the outlet, demonstrating the cumulative effect of evaporation throughout the tube bank.

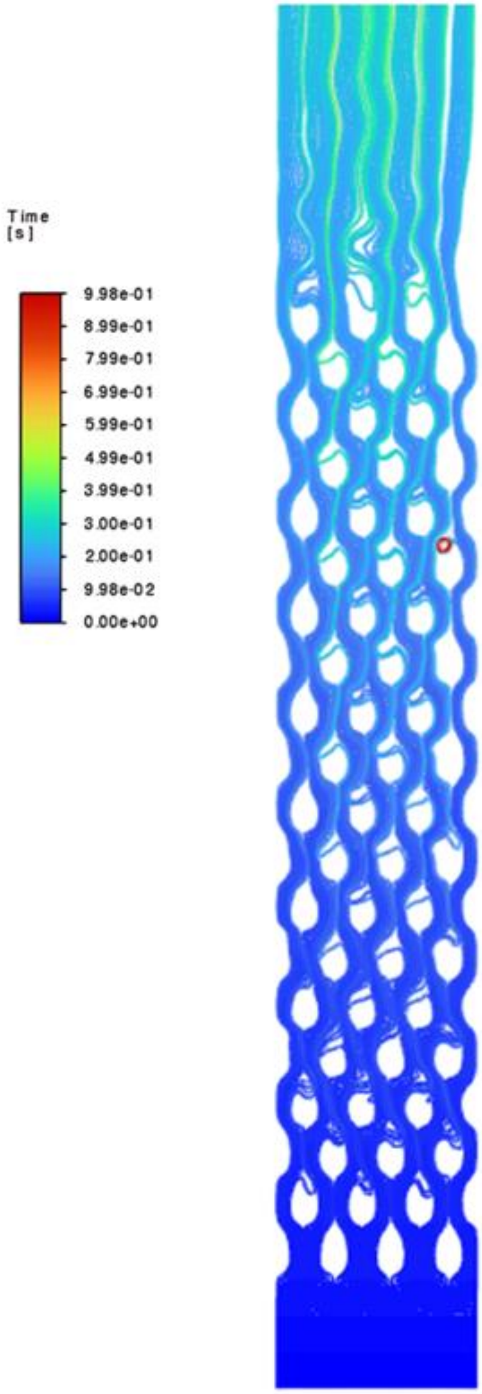

Figure 3.10 : Pathlines around the serpantine tubes.

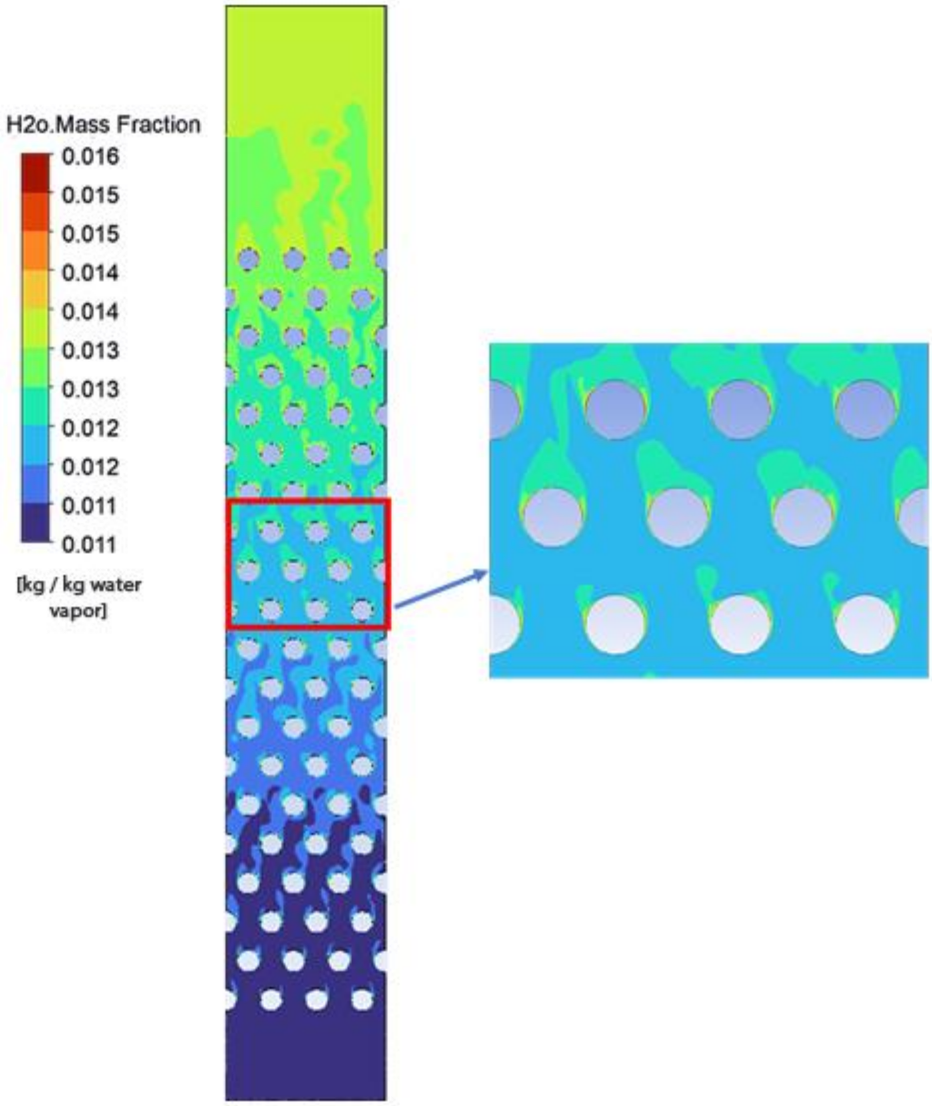

Figure 3.11 : Mass fraction of water vapor contours around the serpentine tubes**.**

The highest concentrations of water vapor are found in the thin boundary layers immediately surrounding the tube surfaces. This strongly indicates that the tube surfaces are the source of the water vapor, representing the evaporation from a liquid film. The turbulent flow effectively mixes the evaporated water into the main air stream, visualizes how the fluid dynamics are directly coupled to and facilitate the mass transfer from the tubes to the air.

Figure 3.12 presents the gauge pressure distribution throughout the serpentine tube bank, with pressure values given in Pascals. A clear and significant pressure drop is observed across the entire domain, decreasing along the direction of flow from the inlet to the outlet. Region exhibits the pressure, approximately 308 Pa which represents the force required to drive the air through the coil assembly.

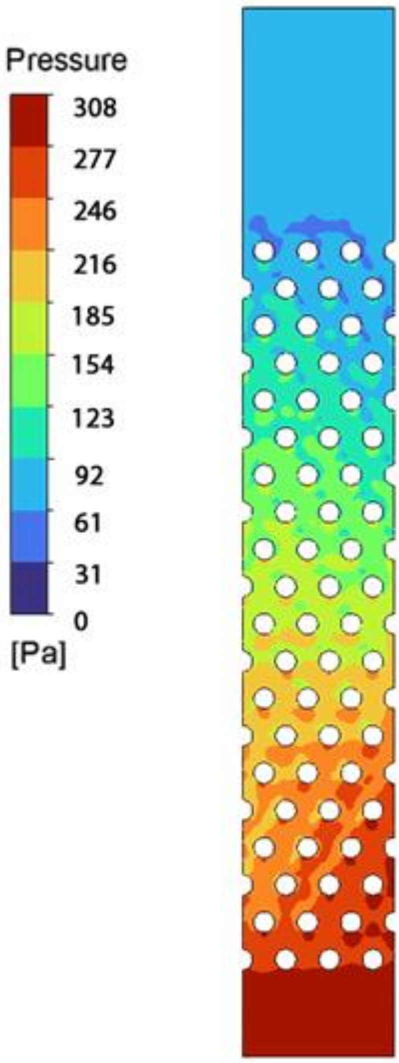

Figure 3.12 : Pressure drop throughout the serpentine tubes.

Figure 3.13 presents the temperature distribution surrounding the serpentine tube banks. The highest temperatures are observed adjacent to the tube surfaces, represented by red and orange shades, which gradually decline into the green and blue regions farther away from the walls. This gradient confirms effective convective heat transfer between the hot tube walls and the moist air.

The visible temperature contours supports the efficiency of the wall-film model employed at the tube surfaces, where water droplets deposit, form a liquid film, and subsequently undergo phase change. The technical data obtained from the results are presented in Table 3.1.

The simulation results demonstrate a slight agreement with experimental data, indicating that the developed CFD model provides a reliable representation of the physical process. The convective heat transfer coefficient between the spray water and tube was found to be 1430 $W/m^2 \cdot K$ in the CFD results, compared to 1163 $W/m^2 \cdot K$ in the experiments, corresponding to a deviation of approximately 23%. This differance is primarily attributed to the insufficient evaporation occurring within the water film, which limited the cooling of both the air stream and the liquid film, thereby reducing the overall heat and mass transfer effectiveness. Additionally, the make-up water flow rate due to evaporation and blowdown was calculated as 0.31 m^3/h in the simulation, whereas the experimental value was 0.54 m^3/h, with a deviation of 43%. These deviations confirm that the CFD model requires a more comprehensive three-dimensional approach for further simulations.

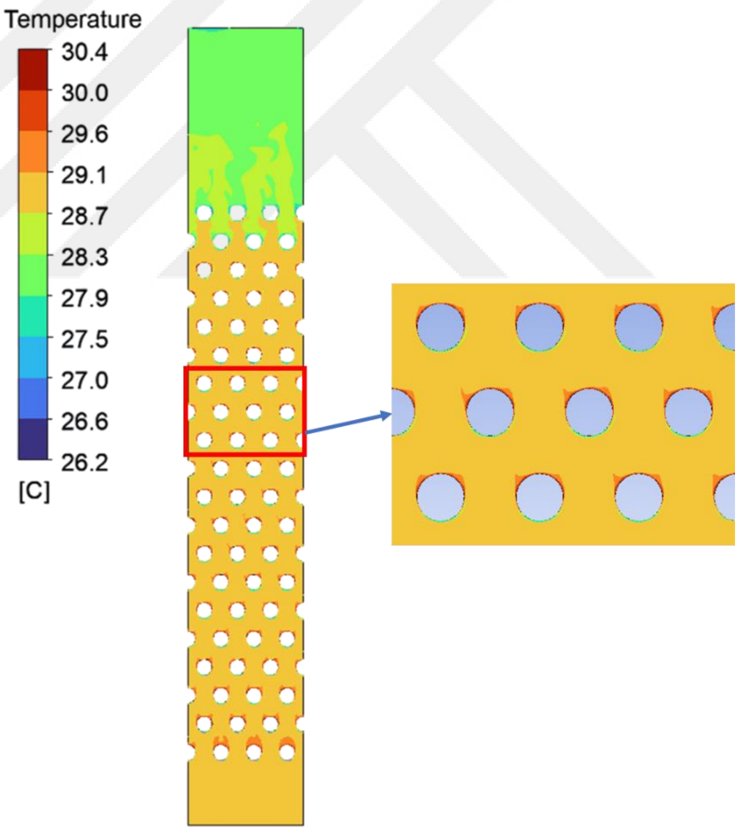

Figure 3.13 : Temperature contours around the serpentine tubes.

Table 3.1 : Summary of CFD DPM 2D model technical data.

Name	Data
Total Wet Surface Area Ratio (%)	%100
Evaporation Loss (kg/s)	0.061
Blowdown Loss (kg/s)	0.024
Makeup Flow (m^3/h)	0.31
Inlet Specific Humidity (kg/kg vapor)	1.09×10^{-2}
Outlet Specific Humidity (kg/kg vapor)	1.25×10^{-2}
Inlet Air Temperature (°C)	29.0
Outlet Air Temperature (°C)	27.9
Wall Film Temperature (°C)	28.8
Serpentine Wall Total Heat Flux (W/m^2)	2497
Spray Water - Tube Heat Transfer Coefficient (W/m^2.K)	1430
Simulation Time (s)	1

3.2.3 3D discrete phase model CFD simulation results

The velocity magnitude contours from the 3D transient simulation of airflow across the serpentine tube bank are shown in Figure 3.14 at a simulation time of 0.5 s. Compared to the 2D case, the velocity field reveals longitudinally developing velocity contours along the tube bundle. The velocity distribution, ranging from 0 to approximately 15 m/s, again exhibits the highest fluid speeds in the narrow passages between the tubes. Furthermore, Figure 3.15 and 3.16 illustrates the corresponding streamlines and pathlines, providing additional insight into the flow behavior.

The no-slip boundary condition is clearly observed at the tube walls, where the velocity drops to zero. These unsteady, three-dimensional turbulent structures play a major role in disturbing the boundary layers and enhancing heat and mass transfer in the cooling tower coil section.

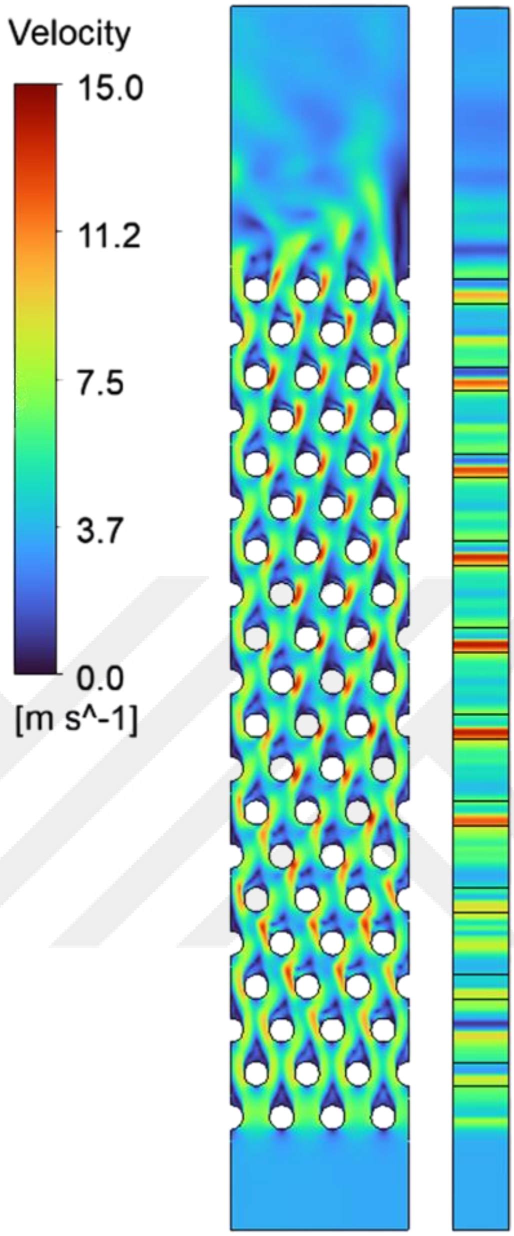

Figure 3.14 : Velocity contours across the serpentine tubes obtained from the 3D simulation.

Figure 3.17 illustrates the mass fraction contours of water vapor within the 3D domain. The air enters with a baseline H_2O mass fraction of 1.09×10^{-2}, and as it progresses upward through the tube bank, it entrains additional vapor evaporated from the water film. Unlike the 2D results, the 3D simulation shows lateral non-uniformities and localized plume structures caused by spanwise vortical motion, which promote a more efficient dispersion of the evaporated vapor. The gradual transition of color from dark blue at the inlet to cyan and light green at the outlet highlights the cumulative evaporation process.

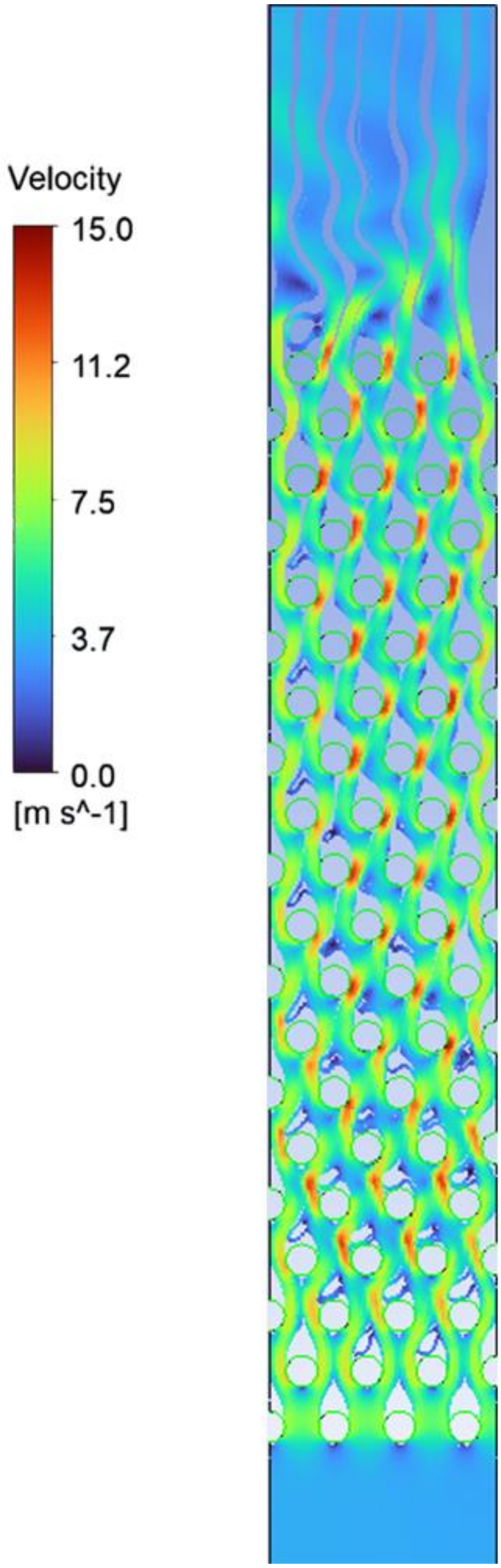

Figure 3.15 : Streamlines around the serpantine tubes obtained from the 3D simulation.

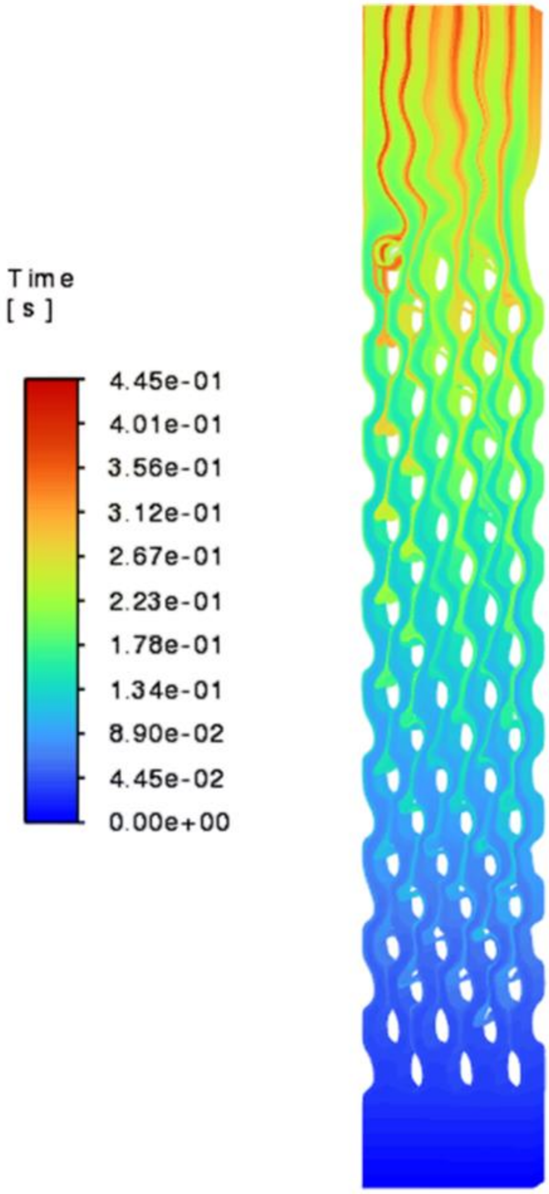

Figure 3.16 : Pathlines around the serpantine tubes obtained from the 3D simulation.

Figure 3.18 illustrates detailed close-up views again confirm that the highest vapor concentrations are located adjacent to the tube surfaces, corresponding to evaporation from the liquid film layer. The turbulent three-dimensional flow promotes rapid mixing of this vapor into the bulk air stream, visualizing the strong coupling between hydrodynamics and mass transfer.

The pressure distribution across the serpentine tube bank is shown in Figure 3.19. As in the 2D case, a distinct pressure drop occurs between the inlet and outlet, with an average reduction of approximately 316 Pa. However, the 3D simulation captures more localized pressure gradients around tube corners and wake regions, better reflecting the physical resistance experienced by air flowing through an actual coil bank.

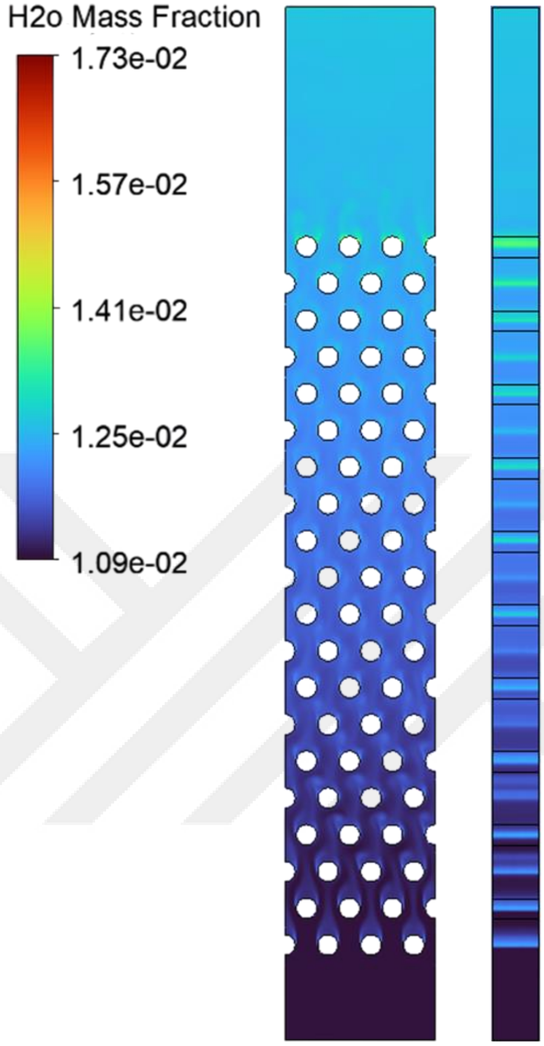

Figure 3.17 : Water vapor mass fraction contours across the serpentine tubes obtained from the 3D simulation.

The temperature contours presented in Figure 3.20 further highlight the convective heat transfer characteristics. The highest temperatures occur along the heated tube walls, gradually decreasing toward the bulk air. In contrast to the 2D analysis, plume-like structures in the 3D case exhibit stronger lateral spreading and interaction between adjacent rows, leading to more temperature drop across the serpentine tubes. This provides additional evidence of the efficiency of the film-evaporation model implemented on the coil surfaces.

Figure 3.21 illustrates detailed close-up views confirm that the lowest air temperatures occur bottom of the tube surfaces, where evaporation from the liquid film layer takes place.

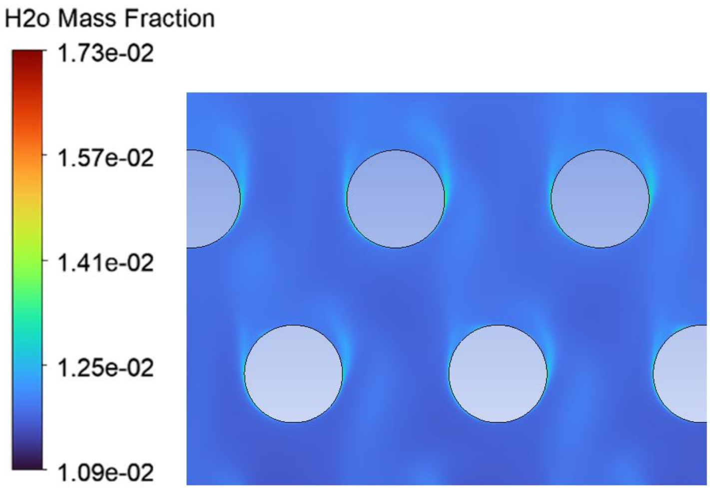

Figure 3.18 : Water vapor mass fraction contours around the serpentine tubes obtained from the 3D simulation.

The quantitative results of the 3D simulation are summarized in Table 3.2. The convective heat transfer coefficient between the spray water and tube wall was calculated as 1526 W/m²·K, compared to the experimental value of 1163 W/m²·K, deviation of about 30%. The make-up water flow rate due to evaporation was predicted as 0.44 m³/h versus 0.54 m³/h in the experiments, yielding a deviation of 29%. When the 3D and 2D models are compared under same initial conditions, the 3D solution produces a greater temperature drop around the serpentine tubes and yields a higher heat flux. Likewise, the 3D model exhibits more film evaporation than the 2D. Given the available computational resources, refining the near-wall mesh resolution would be expected to further improve the agreement for both the spray water–tube heat transfer coefficient and the predicted make-up water rate.

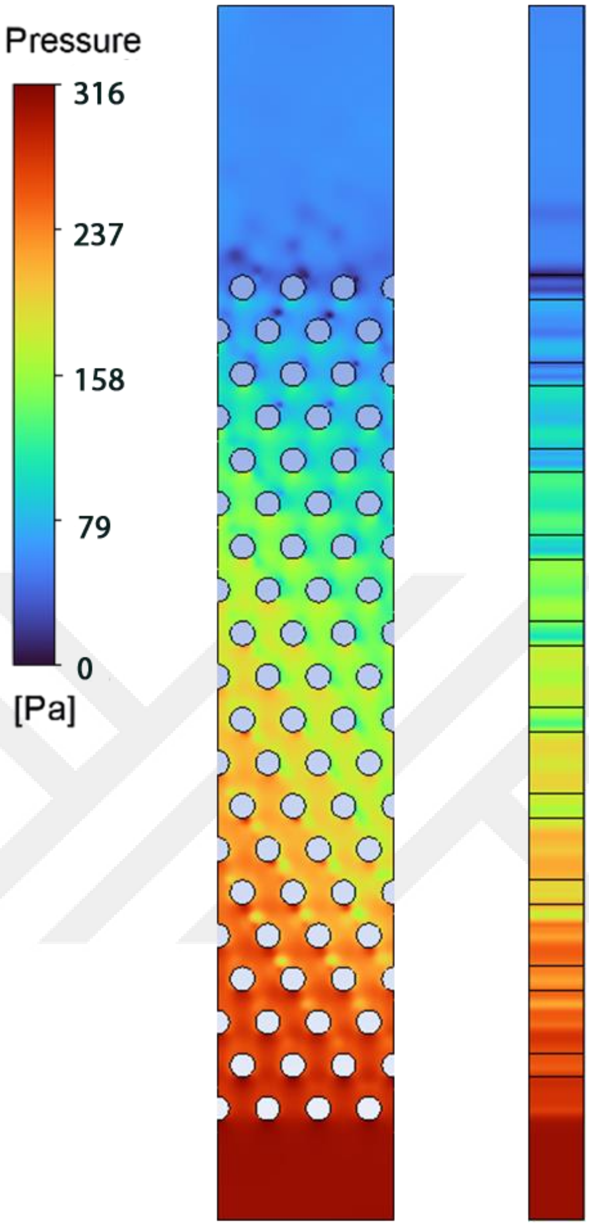

Figure 3.19 : Pressure contours across the serpentine tubes obtained from the 3D simulation.

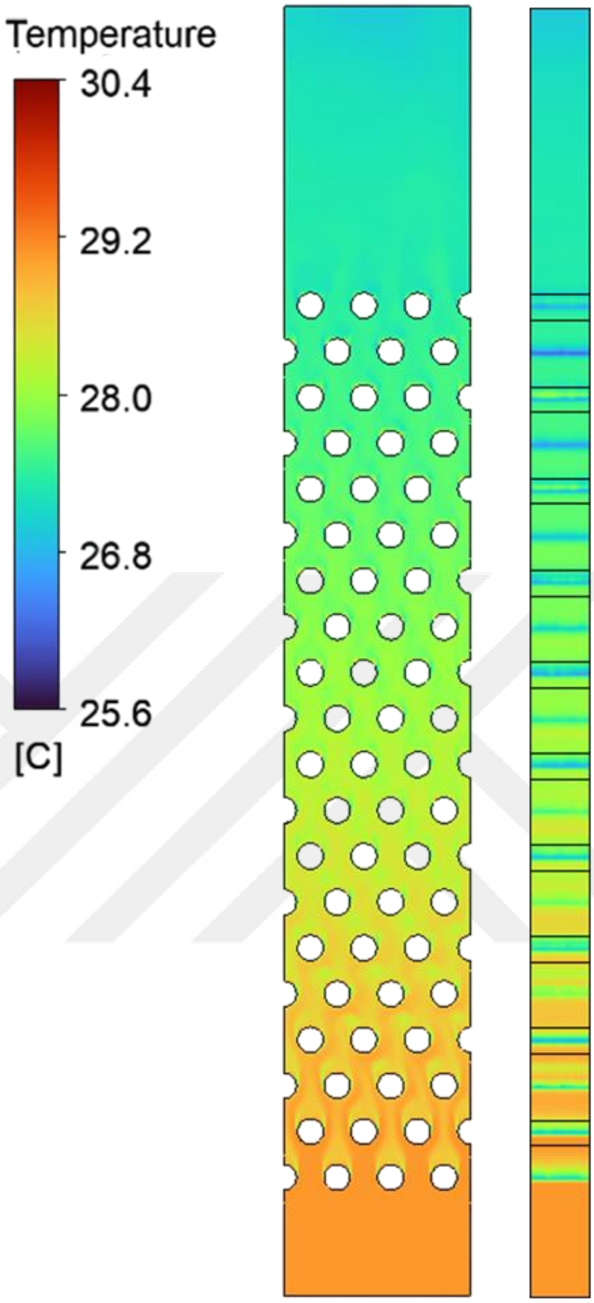

Figure 3.20 : Temperature contours across the serpentine tubes obtained from the 3D simulation.

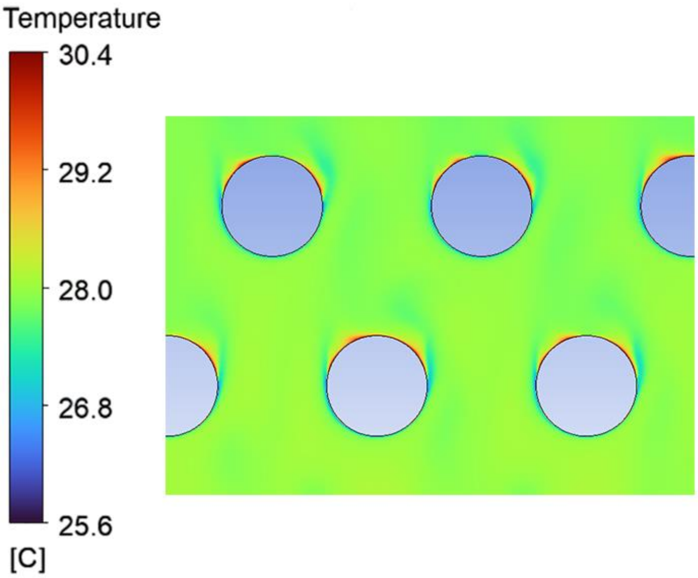

Figure 3.21 : Temperature contours around the serpentine tubes obtained from the 3D simulation.

Table 3.2 : Summary of CFD DPM 3D model technical data.

Name	Data
Total Wet Surface Area Ratio (%)	%83
Evaporation Loss (kg/s)	0.087
Blowdown Loss (kg/s)	0.035
Makeup Flow (m^3/h)	0.44
Inlet Specific Humidity (kg/kg vapor)	1.09×10^{-2}
Outlet Specific Humidity (kg/kg vapor)	1.32×10^{-2}
Inlet Air Temperature (°C)	29.0
Outlet Air Temperature (°C)	27.0
Wall Film Temperature (°C)	27.4
Serpentine Wall Total Heat Flux (W/m^2)	5128
Spray Water - Tube Heat Transfer Coefficient (W/m^2.K)	1526
Simulation Time (s)	0.5

4. CONCLUSION

4.1 Summary of Findings

This study aimed to investigate the thermal and fluid dynamic behavior of a packaged-type closed-circuit cooling tower through both experimental and numerical approaches. The computational analysis incorporated various modeling strategies, including the Mixture multiphase method and the Discrete Phase Model (DPM), in both two- and three-dimensional configurations. The outcomes of these investigations, along with their comparison to experimental observations, provided valuable insights into the mechanisms of heat and mass transfer in evaporative cooling systems.

The key findings obtained throughout the study are summarized below:

(1) The Mixture model tended to overpredict the spray-side heat transfer coefficient and evaporation rate. At an air velocity of 1.5 m/s, the simulated heat transfer coefficient was around 1000 $W/m^2 \cdot K$, whereas the experimentally derived value at 3.5 m/s was approximately 1163 $W/m^2 \cdot K$. This deviation was attributed to the sharp interphase treatment and orifice-shaped inlet, which led to an unrealistic estimation of film thickness and droplet dispersion.

(2) The numerical results of 2D DPM model demonstrated a slight agreement with experimental trends, particularly in terms of temperature profiles, specific humidity. As expected, air velocity increased in the narrower sections, both the temperature and vapor mass fraction rose near the tube surfaces, and a pressure drop was observed from top to bottom.

(3) In 2D DPM model, the make-up water flow rate was calculated as 0.31 m^3/h in the CFD simulation, whereas the experimentally measured value was 0.54 m^3/h, corresponding to a deviation of approximately 43%. This underprediction of moisture content indicates that the evaporation rate within the computational domain was slightly underestimated.

(4) 2D DPM analysis indicates that the total heat flux on the serpentine wall surfaces was calculated as 2497 W/m², which also remained below the experimental estimation. Due to the reduced heat transfer on the tube surfaces, the predicted wall film temperature reached 28.8 °C, compared to 24.7 °C in the experiments, leading to a noticeable temperature deviation between numerical and measured values.

(5) The 3D simulations extended this analysis and revealed important physical effects absent in the 2D approach. Although the heat transfer coefficient is slightly higher compared to the experimental results, the 3D model produced a higher tube-side film temperatures, higher heat fluxes, and stronger evaporation than the 2D under same initial conditions.

(6) Quantitatively, the wall film temperature was predicted as 27.4 °C, the total heat flux on the serpentine wall surfaces reached 5128 W/m², and the spray water–tube heat transfer coefficient was calculated as 1526 W/m²·K, corresponding to an average deviation of approximately 30% from the experimental value.

(7) In 3D model, the make-up water flow rate due to evaporation was predicted as 0.44 m³/h versus 0.54 m³/h in the experiments, yielding a deviation of 29%. This result represents a significant improvement compared to the 2D simulation, indicating that the 3D approach provides a closer estimation of the actual evaporation rate observed experimentally.

(8) Moreover, the 3D model was able to capture non-uniformities such as incomplete wetting, water deflection, and shadow regions behind tubes—phenomena that cannot be resolved in a uniform 2D framework. Despite higher computational demands, three-dimensional modeling is essential for accurate prediction of local heat and mass transfer processes in closed-circuit cooling towers.

(9) From the experimental side, performance indicators such as dry-bulb (29.0 °C) and wet-bulb (19.7 °C) inlet air temperatures, along with water cooling from 34.9 °C to 25.9 °C, confirmed the effectiveness of the cooling system. The corresponding range and approach were calculated as 6.97 °C and 6.17 °C,

respectively. These results validate the experimental setup and provide a benchmark for CFD calibration.

In conclusion, this research delivers valuable insight into the heat and mass transfer mechanisms occurring in CCCTs and underscores the critical interplay between numerical modeling and experimental validation. The findings offer practical guidance for the thermal design and performance optimization of evaporative cooling systems in industrial applications, with future work aimed at developing more comprehensive 3D models and incorporating droplet dynamics for improved prediction fidelity.

4.2 Future Work

Although the current study successfully demonstrated the numerical modeling of heat and mass transfer mechanisms in a closed-circuit cooling tower using multiphase and discrete phase models, several improvements and extensions are possible for future research.

First, the turbulence modeling approach could be expanded beyond the Realizable k-omega employed in this work. Advanced turbulence models such as Reynolds Stress Model (RSM) or Large Eddy Simulation (LES) could be implemented to better capture unsteady vortex shedding, secondary flows, and anisotropic turbulence effects around the serpentine tube bundles.

Second, regarding the droplet injection and breakup modeling, the KHRT model used here can be compared with alternative breakup models, such as TAB or Wave models, to evaluate their influence on droplet size distribution, film formation, and evaporation rate. Moreover, instead of simplified surface injection, a cone-type injection with a prescribed spray angle could be employed to introduce more realistic non-uniformity and enhance the representation of practical spray behavior inside the tower.

Third, future work could involve comparing the numerical results with a broader range of experimental datasets obtained under different operating conditions, such as varying spray flow rates, air velocities, and inlet temperatures. Such comparisons would provide a more comprehensive assessment of model reliability and identify limitations specific to certain regimes. Conducting multiple experimental validations, rather than relying on a single case, would significantly improve the robustness and general applicability of the numerical model.

Additionally, future studies may focus on coupled thermal-hydrodynamic effects, such as variable film temperature along the flow path, phase change-driven interfacial deformation, or transient evaporation–condensation cycles. Including radiation effects and more detailed species diffusion models could also improve the accuracy of multiphase interaction predictions.

Finally, extending the model to a full-scale 3D transient configuration with experimentally validated boundary conditions would enable a more comprehensive understanding of the complex interactions between air, water droplets, and tube surfaces. Such an approach would bridge the gap between laboratory-scale CFD models and industrial-scale cooling tower performance predictions.

REFERENCES

[1] **Gan, G., Riffat, S.B.** (1999). "Numerical simulation of closed wet cooling towers for chilled ceiling systems." Applied Thermal Engineering, Vol. 19, No. 12, pp. 1279–1296. ISSN 1359-4311.

[2] **Gan, G., Riffat, S.B., Shao, L., Doherty, P.** (2001). "Application of CFD to closed-wet cooling towers." Applied Thermal Engineering, Vol. 21, No. 1, pp. 79–92. ISSN 1359-4311.

[3] **Qiu, Q., Jiang, W., Shen, S., Zhu, X., Mu, X.** (2015). "Numerical investigation on characteristics of falling film in horizontal-tube falling film evaporator." Desalination and Water Treatment, Vol. 55, No. 12, pp. 3247–3252. ISSN 1944-3986.

[4] **Chen, J., Zhang, R., Niu, R.** (2015). "Numerical simulation of horizontal tube bundle falling film flow pattern transformation." Renewable Energy, Vol. 73, pp. 62–68. ISSN 0960-1481.

[5] **Fiorentino, M., Starace, G.** (2016). "Numerical investigations on two-phase flow modes in evaporative condensers." Applied Thermal Engineering, Vol. 94, pp. 777–785. ISSN 1359-4311.

[6] **Xie, X., He, C., Xu, T., Zhang, B., Pan, M., Chen, Q**. (2017). "Deciphering the thermal and hydraulic performances of closed wet cooling towers with plain, oval and longitudinal fin tubes." Applied Thermal Engineering, Vol. 120, pp. 203–218. ISSN 1359-4311.

[7] **Xie, X., He, C., Zhang, B., Chen, Q.** (2018). "Heat transfer enhancement for the coil zone of closed wet cooling towers through field synergy analysis." In: Eden, M.R., Ierapetritou, M.G., Towler, G.P. (Eds.), Computer Aided Chemical Engineering, Vol. 44, pp. 1927–1932. Elsevier. ISSN 1570-7946.

[8] **Xie, X., Liu, H., He, C., Zhang, B., Chen, Q., Pan, M.** (2019). "Deciphering the heat and mass transfer behaviors of staggered tube bundles in a closed wet cooling tower using a 3-D VOF model." Applied Thermal Engineering, Vol. 161, 114202. ISSN 1359-4311.

[9] **Zhao, G., R., Bu, S., Zhao, X., Zhang, L., Xu, W., Yu, Z., Fang, J., Ji, Y., Hu, Y., Bao, B.** (2021). "Study on thermal performance of new finned heat exchange tube bundles in cooling tower." International Journal of Thermal Sciences, Vol. 168, 107064. ISSN 1290-0729.

[10] **Liu, H., Wu, Z., Zhang, B., Chen, Q., Pan, M., Ren, J., He, C.** (2023). "A large-scale stochastic simulation-based thermodynamic optimization for the hybrid closed circuit cooling tower system with parallel computing." Energy, Vol. 283, 128434. ISSN 0360-5442.

[11] **Heyns, J.A., Kröger, D.G.** (2010). "Experimental investigation into the thermal-flow performance characteristics of an evaporative cooler." Applied Thermal Engineering, Vol. 30, No. 5, pp. 492–498. ISSN 1359-4311.

[12] **Wickert, D., Prokop, G.** (2021). "Simulation of water evaporation under natural conditions—A state-of-the-art overview." Experimental and Computational Multiphase Flow, Vol. 3, pp. 242–249.

[13] **Kröger, D. G**. (2004). Air-cooled heat exchangers and cooling towers: Thermal-flow performance evaluation and design, Vol. 1, PennWell Corporation, pp. 282-290.

[14] **Poppe, M., Rögener, H.** (1993). *Evaporative Cooling Systems*. VDI-Wärmeatlas, Section Mh.

[15] **Merkel, F. (1925).** "Verdunstungskühlung." *VDI Zeitschrift*, Vol. 70, pp. 123–128.

[16] **Mizushina, T., Ito, R., Miyasita, H.** (1967). "Experimental study of an evaporative cooler." *International Chemical Engineering*, Vol. 7, No. 4, pp. 727–732.

[17] **Parker, R.O., Treybal, R.E.** (1961). "Heat, mass transfer characteristics of evaporative coolers." *AIChE Chemical Engineering Progress Symposium Series*, Vol. 57, No. 32, pp. 138–149.

[18] **Niitsu, Y., Naito, K., Anzai, T.** (1969). "Studies on characteristics and design procedure of evaporative coolers." *Journal of SHASE*, Vol. 43, Japan.

[19] **Wu, Z., Lu, Z., Zhang, B., He, C., Chen, Q., Yu, H., Ren, J.** (2022). "Stochastic bi-objective optimization for closed wet cooling tower systems based on a simplified analytical model." *Energy*, Vol. 250, 123703. ISSN 0360-5442.

[20] **Hassab, M.A., Mansour, M.K., Sadek, L.A., Qassem, M.A.** (2023). "Thermal and experimental analysis of cross-flow closed cooling tower." *Alexandria Engineering Journal*, Vol. 69, pp. 739–746. ISSN 1110-0168.

[21] **Zhao, R., Bu, S., Zhao, X., Zhang, L., Xu, W., Yu, Z., Fang, J., Ji, Y., Hu, Y., Bao, B.** (2021). "Study on thermal performance of new finned heat exchange tube bundles in cooling tower." *International Journal of Thermal Sciences*, Vol. 168, 107064. ISSN 1290-0729.

[22] **Hasan, A., Sirén, K.** (2004). "Performance investigation of plain circular and oval tube evaporatively cooled heat exchangers." *Applied Thermal Engineering*, Vol. 24, Issues 5–6, pp. 777–790. ISSN 1359-4311.

[23] **Papaefthimiou, V.D., Rogdakis, E.D., Koronaki, I.P., Zannis, T.C**. (2012). "Thermodynamic study of the effects of ambient air conditions on the thermal performance characteristics of a closed wet cooling tower." *Applied Thermal Engineering*, Vol. 33–34, pp. 199–207. ISSN 1359-4311.

[24] **Jiang, J.J., Liu, X.H., Jiang, Y**. (2013). "Experimental and numerical analysis of a cross-flow closed wet cooling tower." *Applied Thermal Engineering*, Vol. 61, Issue 2, pp. 678–689. ISSN 1359-4311.

[25] **Navarro, P., Serrano, J.M., Roca, L., Palenzuela, P., Lucas, M., Ruiz, J.** (2024). "A comparative study on predicting wet cooling tower performance in combined cooling systems for heat rejection in CSP plants." *Applied Thermal Engineering*, Vol. 253, 123718. ISSN 1359-4311.

[26] **Facão, J., Oliveira, A.C.** (2000). "Thermal behaviour of closed wet cooling towers for use with chilled ceilings." *Applied Thermal Engineering*, Vol. 20, Issue 13, pp. 1225–1236. ISSN 1359-4311.

[27] **Qu, J., Li, M., He, C., Zhang, B., Chen, Q., Ren, J.** (2022). "Deciphering the optimal exergy field in closed-wet cooling towers using Bi-level reduced-order models." *Energy*, Vol. 238, Part A, 121766. ISSN 0360-5442.

[28] **Zhang, L., Liu, X., Jiang, Y.** (2015). "Exergy analysis of parameter unmatched characteristic in coupled heat and mass transfer between humid air and water." *International Journal of Heat and Mass Transfer*, Vol. 84, pp. 327–338. ISSN 0017-9310.

[29] **Li, W., Li, Y., Shi, W., Lu, J.** (2021). "Energy and exergy study on indirect evaporative cooler used in exhaust air heat recovery." *Energy*, Vol. 235, 121319. ISSN 0360-5442.

[30] **Singh, K., Das, R.** (2017). "Exergy optimization of cooling tower for HGSHP and HVAC applications." *Energy Conversion and Management*, Vol. 136, pp. 418–430. ISSN 0196-8904.

[31] **Meroney, R.N.** (2006). "CFD prediction of cooling tower drift." *Journal of Wind Engineering and Industrial Aerodynamics*, Vol. 94, Issue 6, pp. 463–490. ISSN 0167-6105.

[32] **Al-Waked, R., Behnia, M.** (2006). "CFD simulation of wet cooling towers." *Applied Thermal Engineering*, Vol. 26, Issue 4, pp. 382–395. ISSN 1359-4311.

[33] **Hajidavalloo, E., Shakeri, R., Mehrabian, M.A.** (2010). "Thermal performance of cross flow cooling towers in variable wet bulb temperature." *Energy Conversion and Management*, Vol. 51, Issue 6, pp. 1298–1303. ISSN 0196-8904.

[34] **Chen, Y., Sun, F., Wang, H., Mu, N., Gao, M.** (2011). "Experimental research of the cross walls effect on the thermal performance of wet cooling towers under crosswind conditions." *Applied Thermal Engineering*, Vol. 31, Issues 17–18, pp. 4007–4013. ISSN 1359-4311.

[35] **Blain, N., Belaud, A., Miolane, M.** (2016). "Development and validation of a CFD model for numerical simulation of a large natural draft wet cooling tower." *Applied Thermal Engineering*, Vol. 105, pp. 953–960. ISSN 1359-4311.

[36] **Xia, L., Gurgenci, H., Liu, D., Guan, Z., Zhou, L., Wang, P.** (2016). "CFD analysis of pre-cooling water spray system in natural draft dry cooling towers." *Applied Thermal Engineering*, Vol. 105, pp. 1051–1060. ISSN 1359-4311.

[37] **Raoult, F., Lacour, S., Carissimo, B., Trinquet, F., Delahaye, A., Fournaison, L.** (2019). "CFD water spray model development and physical parameter study on the evaporative cooling." *Applied Thermal Engineering*, Vol. 149, pp. 960–974. ISSN 1359-4311.

[38] **Guo, Q., Qi, X., Sun, P., Guo, P.** (2019). "New explicit analytical solutions of equations for heat and mass transfer in a cooling tower energy system." *Advances in Mechanical Engineering*, Vol. 11, Issue 12, 1687814019896147. ISSN 1687-8140.

[39] **Chen, R., Zhang, D., Zhang, Z., Han, Q., He, S., Gao, M.** (2021). "Numerical study regarding cooling capacity for non-equidistant fillings in large-scale wet cooling towers." *Case Studies in Thermal Engineering*, Vol. 26, 101103. ISSN 2214-157X.

[40] **Zhang, D., Zhang, Z., Han, Q., Wu, F., He, S., Gao, M.** (2021). "Numerical simulation on synergetic optimization of non-equidistant fillings and non-uniform water distribution for wet cooling towers." *International Journal of Heat and Mass Transfer*, Vol. 179, 121676. ISSN 0017-9310.

[41] **Yu, J.H., Qu, Z.G., Zhang, J.F., Hu, S.J., Guan, J.** (2022). "Comprehensive coupling model of counter-flow wet cooling tower and its thermal performance analysis." *Energy*, Vol. 238, Part B, 121726. ISSN 0360-5442.

[42] **Zhang, Z., Wang, M., Wang, Y., He, S., Gao, M.** (2022). "Influences of dry-wet hybrid rain zone on the heat and mass transfer characteristics of wet cooling towers: A case study." *Case Studies in Thermal Engineering*, Vol. 30, 101784. ISSN 2214-157X.

[43] **Yang, J., Jia, Z., Guan, H., He, S., Gao, M.** (2023). "Influence of three different pitches fillings on the cooling performance of wet cooling towers under crosswind." *Applied Thermal Engineering*, Vol. 220, 119760. ISSN 1359-4311.

[44] **Castiglione, T., Nicoletti, F., Ferraro, V., Sangineto, C.M.** (2023). "CFD analysis of Part-Load operation of an Open-Circuit Induced-Draft cooling tower." *Applied Thermal Engineering*, Vol. 229, 120636. ISSN 1359-4311.

[45] **Tissot, J., Boulet, P., Trinquet, F., Fournaison, L., Macchi-Tejeda, H.** (2011). "Air cooling by evaporating droplets in the upward flow of a condenser." *International Journal of Thermal Sciences*, Vol. 50, Issue 11, pp. 2122–2131. ISSN 1290-0729.

[46] **Lacour, S.O.L., Trinquet, F., Vendee, P.E., Vallet, A., Delahaye, A., Fournaison, L.** (2018). "Assessment of the wet area of a heat exchanger exposed to a water spray." *Applied Thermal Engineering*, Vol. 128, pp. 434–443. ISSN 1359-4311.

[47] **Ren, C., Li, N., Tang, G.** (2002). "Principles of exergy analysis in HVAC and evaluation of evaporative cooling schemes." *Building and Environment*, Vol. 37, Issue 11, pp. 1045–1055. ISSN 0360-1323.

[48] **Kanoglu, M., Ozdinç Çarpinlıoğlu, M., Yildirim, M**. (2004). "Energy and exergy analyses of an experimental open-cycle desiccant cooling system." *Applied Thermal Engineering*, Vol. 24, Issues 5–6, pp. 919–932. ISSN 1359-4311.

[49] **Qureshi, B.A., Zubair, S.M.** (2007). "Second-law-based performance evaluation of cooling towers and evaporative heat exchangers." *International Journal of Thermal Sciences*, Vol. 46, Issue 2, pp. 188–198. ISSN 1290-0729.

[50] **Muangnoi, T., Asvapoositkul, W., Wongwises, S.** (2007). "An exergy analysis on the performance of a counterflow wet cooling tower." *Applied Thermal Engineering*, Vol. 27, Issues 5–6, pp. 910–917. ISSN 1359-4311.

[51] **AHRI** (1997). *1997 GUIDELINE for Fouling Factors: A Survey Of Their Application In Today's Air Conditioning And Refrigeration Industry.* Retrieved from https://www.ahrinet.org/system/files/2023-06/AHRI_Guideline_E_1997.pdf

APPENDICES

APPENDIX A: Thermophysical Properties

APPENDIX A.1 The Thermophysical Properties of Air and Water Vapor

APPENDIX A.2 The Thermophysical Properties of Water Liquid

APPENDIX A.1 The Thermophysical Properties of Air and Water Vapor

- Density (kg/m³):

$$\rho_a = \frac{(1 + w)\left(1 - \frac{w}{w + 0.62198}\right)P}{287.08(T_{db} + 273.15)} \tag{A.1.1}$$

w : Specific humidity (kg/kg vapor)

T_{db}: Dry Bulb Temperature (°C)

P : Atmospheric Pressure (Pa)

- Specific Heat of Air (J/kg.K):

$$\begin{aligned} C_{pa} = 1045.356 - 3.161783x10^{-1}(T_{db} + 273.15) \\ + 7.083814x10^{-4}(T_{db} + 273.15)^2 \\ - 2.705209x10^{-7}(T_{db} + 273.15)^3 \end{aligned} \tag{A.1.2}$$

T_{db}: Dry Bulb Temperature (°C)

- Specific Heat of Vapor (J/kg.K):

$$\begin{aligned} C_{pv} = 1360.5 + 2.31334(T_{db} + 273.15) \\ - 2.46784x10^{-10}(T_{db} + 273.15)^5 \\ + 5.91332x10^{-13}(T_{db} + 273.15)^6 \end{aligned} \tag{A.1.3}$$

T_{db}: Dry Bulb Temperature (°C)

- Dynamic viscosity:

$$\begin{aligned} \mu_a = 2.287973x10^{-6} + 6.259793x10^{-8}(T_{db} + 273.15) \\ - 3.131956x10^{-11}\ (T_{db} + 273.15)^2 \\ + 8.15038x10^{-15}\ (T_{db} + 273.15)^3 \end{aligned} \tag{A.1.4}$$

T_{db}: Dry Bulb Temperature (°C)

- Thermal conductivity:

$$k_a = -4.937787x10^{-4} + 1.018087x10^{-4}(T_{db} + 273.15) - 4.627937x10^{-8}(T_{db} + 273.15)^2 + 1.250603x10^{-11}(T_{db} + 273.15)^3 \quad (A.1.5)$$

T_{db}: Dry Bulb Temperature (°C)

- Specific Humidity (kg/kg vapor):

$$w = \frac{\left((2501 - 2.326T_{wb})\frac{0.621945P_{vwb}}{P - P_{vwb}} - 1.006(T_{db} - T_{wb})\right)}{2501 + 1.86T_{db} - 4.186Twb} \quad (A.1.6)$$

T_{db}: Dry Bulb Temperature (°C)

T_{wb}: Wet Bulb Temperature (°C)

P_{vwb}: Saturated Vapor Pressure at Wet Bulb Temperature (°C)

P : Atmospheric Pressure (Pa)

- Enthalpy:

$$i_a = C_{pa}\, T_{db} + w\left(i_{fgwo} + C_{pv}T_{db}\right) \quad (A.1.7)$$

T_{db}: Dry Bulb Temperature (°C)

C_{pa}: Specific Heat of Air (J/kg.K)

C_{pv}: Specific Heat of Vapor (J/kg.K)

w : Specific Humidity (kg/kg vapor)

APPENDIX A.2 The Thermophysical Properties of Water Liquid

- Density (kg/m³):

$$\rho_w = \left((1.49343x10^{-3} - 3.7164x10^{-6}(T_w + 273.15) + 7.09782x10^{-9}(T_w + 273.15)^2 - 1.90321x10^{-20}(T_w + 273.15)^6)\right)^{-1} \quad \text{(A.2.1)}$$

T_w : Water Temperature (°C)

- Specific Heat of Air (J/kg.K):

$$C_{pw} = 8.15599x10^3 - 2.80627x10(T_w + 273.15) + 5.11283(T_w + 273.15)^2x10^{-2} - 2.17582(T_w + 273.15)^6x10^{-13} \quad \text{(A.2.2)}$$

T_w : Water Temperature (°C)

- Dynamic viscosity:

$$\mu_w = 2.414x10^{-5}x10^{\frac{247.8}{T_w + 273.15 - 140}} \quad \text{(A.2.3)}$$

T_w : Water Temperature (°C)

- Thermal conductivity:

$$k_w = -6.14255x10^{-1} + 6.9962x10^{-3}(T_w + 273.15) - 1.01075x10^{-5}(T_w + 273.15)^2 + 4.74737x10^{-12}(T_w + 273.15)^4 \quad \text{(A.2.4)}$$

T_w : Water Temperature (°C)

CURRICULUM VITAE

Name Surname : Efe GÜRLE

EDUCATION :

- **B.Sc.** : 2022, Istanbul Technical University, Mechanical Engineering

PROFESSIONAL EXPERIENCE AND REWARDS:

- 2023-2025 Cenk Industry, Thermal and Project Engineer.